

Ecosystem-relevant Ocean Flux (version 2)

Project acronym:	ATLAS
Grant Agreement:	678760
Deliverable number:	D1.2
Deliverable title:	Ecosystem-relevant Ocean Flux
Work Package:	1
Date of completion:	January 2020
Author:	Clare Johnson, Mark Inall, Stefan Gary, Stuart Cunningham



This project has received funding from the European Union's Horizon 2020 research and innovation programme under grant agreement No 678760 (ATLAS). This output reflects only the author's view and the European Union cannot be held responsible for any use that may be made of the information contained therein.

Contents

Executive summary.....	4
Changes from version 1	5
1. Introduction.....	6
2. Data.....	8
2.1 VIKING20	8
2.2 EN4	9
2.3 Climate indices.....	10
2.3.1 Strength of Atlantic Meridional Overturning Circulation (AMOC).....	10
2.3.2 North Atlantic Oscillation (NAO)	11
2.3.3 Atlantic Multi-decadal Oscillation.....	11
2.3.4 Strength of subpolar gyre (SPG).....	11
3. Results: Long term mean state.....	12
3.1 Atlantic-wide.....	12
3.1.1 VIKING20	12
3.1.2 EN4	18
3.2 ATLAS case study sites	19
3.2.1 VIKING20	19
3.2.2 EN4	19
4. Results: Seasonal variability	22
4.1 VIKING20	22
4.2 EN4	26
5. Temporal variability of climate indices	28
6. Results: Spatial variability linked to AMOC states	31
6.1 VIKING20	32
6.2 EN4	36
7. Results: Spatial variability linked to NAO states	38

7.1 VIKING20	39
7.2 EN4	42
8. Results: Spatial variability linked to SPG states.....	44
9. Results: Spatial variability linked to AMO states.....	46
10. Variability at case study sites.....	49
10.1 VIKING20	49
10.2 EN4	52
11. Discussion and summary	55
Acknowledgements.....	58
Appendix A: Seasonal signal of climate indices.....	59
Appendix B: Variability associated with climate indices in VIKING20.....	62
Appendix C: Variability associated with climate indices in EN4.....	76
References.....	90

Executive summary

An overarching goal of ATLAS is to investigate the sensitivity of North Atlantic Ocean ecosystems to basin-scale physical processes. This report examines relationships between four pertinent climate indices and key physical variables using both output from a high-resolution ocean model and an observational dataset.

After describing long-term mean conditions and determining seasonal cycles, we use a composite approach to create mean conditions for high and low states of each climate index.

The Atlantic Meridional Overturning Circulation (AMOC) shows cooler bottom conditions around the boundaries of the western subpolar gyre during a high state, which may be linked to more energetic conditions in this area.

The North Atlantic Oscillation (NAO) shows clear anti-correlation between European and North American Shelves: during a high NAO, bottom conditions on the eastern boundary are warmer and more saline, whilst western areas are cooler and fresher. Bottom kinetic energy also shows an east-west disconnect, with less energetic conditions in the eastern overflow currents during a high NAO and a corresponding increase in western overflows.

The most striking feature in the Subpolar Gyre (SPG) composites, is a strong area of cooler bottom conditions around the northern and western boundaries of the subpolar North Atlantic during a high SPG. In contrast, during a high Atlantic Multi-decadal Oscillation (AMO), bottom conditions in the same areas are warmer and more saline although areas deeper than around 2000 m in the North Atlantic are cooler and fresher.

This is the first study to show that climate indices are associated with spatially-coherent changes in bottom conditions across the North Atlantic region. Although changes are relatively small, due to the multi-annual nature of the climate indices any changes may persist for several years. As such, vulnerable sessile ecosystems may be exposed to sustained changes in mean conditions, with this deviation in the baseline also altering the likelihood of extreme events such as mean heatwaves.

Thus, a thorough knowledge of natural variability is essential for the understanding of deep-sea ecosystems, predicting their response to future changes, and evaluation of management frameworks.

Changes from version 1

This report is updated from version 1. Changes include:

- (1) Completion of section 3.2.2
- (2) Completion of section 4.2
- (3) Completion of 10.2
- (4) Addition of appendix C
- (5) Addition of executive summary
- (6) Addition of labels to multi-panel plots
- (7) Re-working of section 10.1

1. Introduction

One of the overarching goals of ATLAS is to investigate the sensitivity of North Atlantic Ocean ecosystems to the seasonal-decadal temporal variability of basin-scale physical processes. Here, we present relationships between climate indices and key physical variables from both historical observations and the output of a cutting-edge, high-resolution ocean model. Since it is important to examine changes over the whole North Atlantic as well as representative ecosystems, we construct basin-scale maps in addition to time series at each of the ATLAS Case Study sites (Figure 1; Table 1). As the heterogeneous, patchy nature of deep ocean ecosystems is generally at a smaller scale than available observations or the topography of the ocean circulation model, we view the extent of each ATLAS case study as an ecosystem.

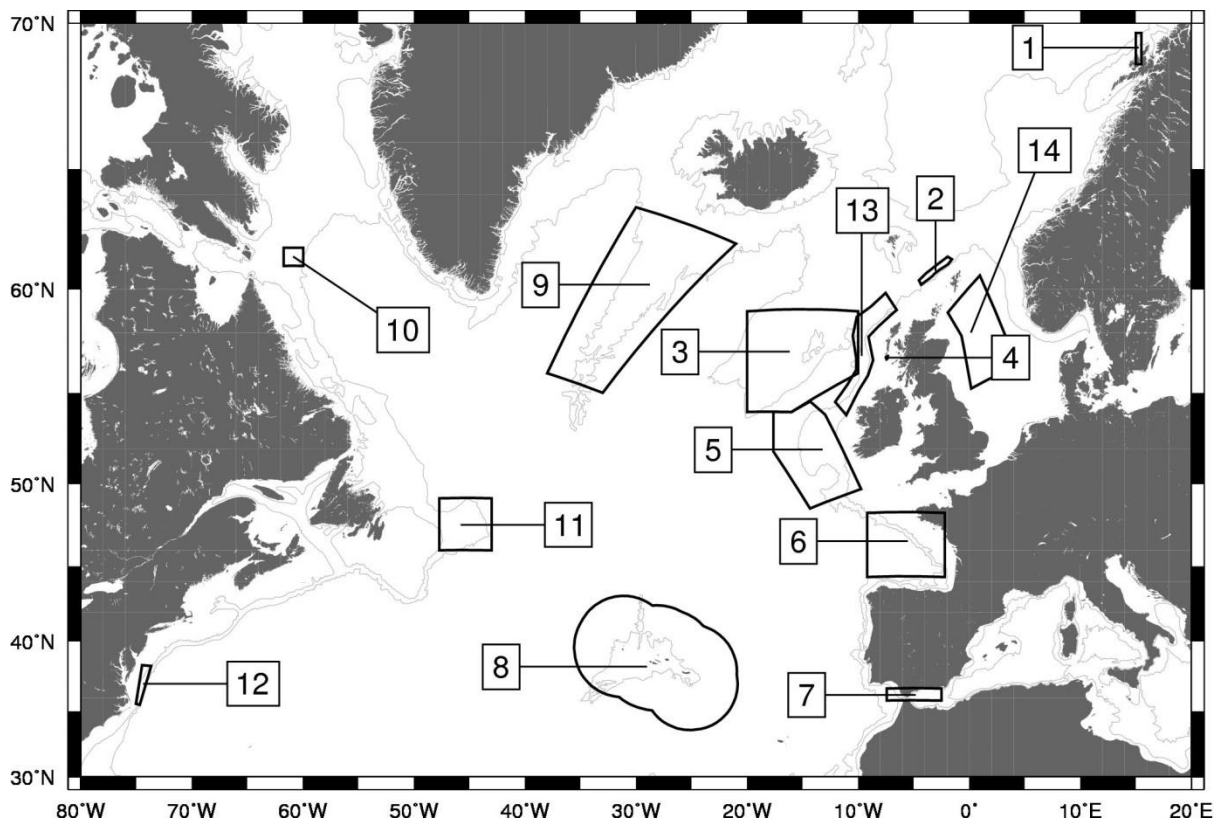


Figure 1. Map of the ATLAS Case Studies (1-12) plus two additional case studies to investigate variability in the European Slope Current (13-14).

The 200m and 2000m isobaths are shown with grey lines; closed contours with a small number of data points are omitted for clarity.

Table 1 Descriptors of case study regions in this report.

All statistics exclude areas of land and were calculated from ETOPO2 bathymetry data. Note that there are considerable differences in the size of the CS regions.

Case Studies	Area (10 ³ km ²)	Mean depth (m)	Min. depth (m)	Max. depth (m)
1 LoVe Observatory	2.2	746	1	2298
2 Western Scottish Slope	5.3	596	234	952
3 Rockall Bank	301.4	1470	21	3026
4 Mingulay Reef	0.1	196	148	230
5 Porcupine Sea Bight	218.2	2187	39	4844
6 Bay of Biscay	238.5	2744	1	5026
7 Gulf of Cadiz / Alboran Sea	43.4	697	1	1872
8 Azores	954.2	3064	1	5627
9 Reykjanes Ridge	388.1	1927	499	3209
10 Davis Strait	8.2	962	518	2319
11 Flemish Cap	124.4	1471	128	4664
12 USA Mid-Atlantic Canyons	16.5	750	32	2205
13 Scottish Slope	61.2	1243	57	3009
14 North Sea	112.0	99	40	179

For this report, we consider four basin-scale physical processes pertinent to the North Atlantic region: the strength of the Atlantic Meridional Overturning Circulation (AMOC); the winter North Atlantic Oscillation (NAO); the Atlantic Multi-decadal Oscillation (AMO); and the strength of the subpolar gyre (SPG). The AMOC magnitude is a measure of the strength of overturning in the North Atlantic. This circulation comprises of a shallow, warm, northward flow balanced by a southward, cold return flow at depth. The NAO, on the other hand, is an atmospheric index spanning the North Atlantic that influences the position and strength of westerly winds (Hurrell, 1995). The NAO has also been shown to affect sea surface temperatures (Visbeck *et al.*, 2013), the position of the Gulf Stream (Joyce *et al.*, 2000) and depth of convection in the Labrador Sea (Dickson *et al.*, 1996). The AMO describes a natural cycle in sea surface temperatures in the North Atlantic with a periodicity of 65-80 years and range of 0.4 °C (Kerr, 2000). The strength of the SPG determines its westward extent and therefore the distribution of water masses in the subpolar North Atlantic. Temperature, salinity and nutrient concentrations in the upper waters have been shown to be related to the SPG index (Hátún

et al., 2017; Hátún *et al.*, 2005; Johnson *et al.*, 2013). It should be noted that although we consider each climate index individually (to examine any similarity in patterns and to enable comparison to other research), they are likely to influence and interact with one another. For example, the SPG index has, at times, been shown to correlate with the NAO index (Lozier and Stewart, 2008), whilst variations in the AMOC has been linked to changes in Atlantic sea surface temperatures (Buckley and Marshall, 2016).

In order to provide a baseline for interpreting temporal changes, we first present the long-term mean and associated variability both as Atlantic-wide maps and averaged over each case study area (sections 3 and 4). The key physical variables extracted from the cutting-edge model, VIKING20, are sea surface height (SSH), sea surface temperature (SST), mixed layer depth (MLD), bottom potential temperature (T_{bot}), bottom salinity (S_{bot}), and bottom kinetic energy (KE_{bot}). For the observational dataset, we use the UK Meteorological Office's EN4 product and focus on bottom potential temperature and salinity. Next, we describe the climate indices (section 5) before using the composite method to create basin-scale maps of the core physical variables (sections 6-9). This method has already been used to show a relationship between the AMOC and SST (Duchez *et al.*, 2016) and here we extend the idea to include the NAO, AMO and SPG in addition to the AMOC, as well as exploring signals at the seabed. Finally, in section 10 we consider the case studies individually, investigating which climate index has the greatest effect for each area. We point the ATLAS case study leaders particularly to sections 3, 4 and 10.

2. Data

The sparse nature of ocean observations, especially at depth, means that we consider an eddy-resolving, hindcast-forced, ocean-only model (VIKING20) in addition to an observational dataset (EN4). We consciously did not use ocean reanalysis products because of their wide-spread.

2.1 VIKING20

Bottom potential temperature (T_{bot}), bottom salinity (S_{bot}), sea surface height (SSH), sea surface temperature (SST), mixed layer depth (MLD), and bottom horizontal velocity (u_{bot} , v_{bot}) fields come from the VIKING20 configuration (Böning *et al.*, 2016) of the NEMO ocean model (Madec, 2008). In the VIKING20 hindcast run, forced by the CORE2 data (Large and Yeager, 2009), a $1/20^\circ$ resolution grid spanning the North Atlantic was two-way nested (Debreu *et al.*, 2008) within a 0.25° resolution

global ocean. VIKING20 output from 1959 to 2009, with a temporal resolution of five day averages is used here.

Due to the staggered grids of the model and the ultimate goal of studying kinetic energy rather than velocity, u and v were first linearly interpolated from their respective grids onto the grid containing T_{bot} and S_{bot} . Then, bottom values, defined as the data from the deepest depth point at each grid point, were found (u_{bot} and v_{bot}). Although these data technically come from the centre of the deepest grid box, they are interpreted as representative of bottom data because of the limits of vertical resolution. For T_{bot} and S_{bot} , using box-centre data is not likely to have a significant impact especially in the weakly stratified deep waters. However, since grid boxes can be up to $\sim 250\text{m}$ thick in the deepest parts of the model domain, real-world, smaller-scale frictional effects in the velocity field are not included in this analysis.

Mean bottom KE was computed as the magnitude of the time-mean mean horizontal velocity along the bottom:

$$mean\ KE = \overline{u_{bot}}^2 + \overline{v_{bot}}^2$$

where the overline indicates the time-mean.

The eddy KE was computed as the sum of the variances of the zonal and meridional velocities:

$$eddy\ KE = var(u_{bot}) + var(v_{bot})$$

Time series of the core variables at each case study site were constructed by averaging all data in each case study polygon (Figure 1) at each five-day time step in the VIKING20 model output. The curvilinear model grid, in which grid boxes have different horizontal extents, required area-weighted averages for each case study area.

2.2 EN4

EN4 is a global quality-controlled dataset of monthly objective-analysis of potential temperature and salinity profiles. It combines data from all types of profiling instruments including Argo floats (Good *et al.*, 2013). Although data is available as monthly averages from 1900 onwards, we limit our analysis from 1959 onwards to match with VIKING20 and to take into account the reduced data availability prior to the 1960s. However, we extend the analysis to the present day (rather than ending in 2009) in order to include as much data as possible.

Potential temperature and salinity data were taken from the deepest data point at each grid-point. The depth of the vertical grid in EN4 varies with water depth, ranging from 10 m bin depths in the upper 100 m to 280 m bin depths at 2000 m. This is not dissimilar to the VIKING20 vertical grid and the same limitations apply. Case study means were computed by simply averaging over all data-points within each case study region. As EN4 has a $1^\circ \times 1^\circ$ resolution, case study 4 did not have a grid-point within its boundaries. In this case, the nearest grid point to the case study site was used. Finally, EN4 weighting values, which represent the amount of data present at a particular location and range from approximately 0 (no data) to 1 (full data), were used to remove periods with sparse or no data. A 5 % cut-off level was chosen with any periods with less than this being considered as having no data and thus not being included in analyses.

2.3 Climate indices

In order to explore variability in the North Atlantic, we examine changes associated with four climate indices pertinent to the region.

2.3.1 Strength of Atlantic Meridional Overturning Circulation (AMOC)

We consider four AMOC time series: one extracted from the VIKING20 model, and three observationally based indices. The VIKING20 AMOC time series was computed by taking the zonal integral of all meridional velocities within the model, and then finding the maximum value of the vertically integrated volume flux starting at the sea surface. Since the ATLAS case studies span a wide range of latitudes, the VIKING20 AMOC was averaged over around 35°N to 60°N to produce a single mean time series. As the AMOC shows some level of meridional coherency over these latitude bands in VIKING20 (Böning *et al.*, 2016), this mean index is broadly similar to the AMOC at any specific latitude. The 5-day average AMOC time-series was averaged to calculate monthly means.

As model results suggests meridional coherence in the AMOC signal breaks down at around 35°N (Böning *et al.*, 2016), we consider observational time series for both the subtropical and subpolar North Atlantic separately. The subtropical index was obtained from the RAPID monitoring array at 26°N (Smeed *et al.*, 2017) and was downloaded from http://www.rapid.ac.uk/rapidmoc/rapid_data/transport.php. This is available from 2004 to present as five-daily averages. The transport time series at 26°N has been extended back to 1993 using altimetry (Frajka-Williams, 2015). This time series extension, which has had seasonal anomalies removed before being smoothed with a 1.5 year Tukey filter, was kindly provided by Elanor Frajka-Williams (NOC).

Two observational datasets exist for the subpolar North Atlantic, one along the OVIDE hydrographic section between Greenland and Portugal, and one along the OSNAP section between Greenland and Scotland. The OVIDE AMOC estimate is defined as the maximum in the overturning stream function and was calculated by combining AVISO altimetry data with ISAS temperature and salinity data (Mercier *et al.*, 2015). The time series was downloaded from <http://www.seanoe.org/data/00353/46445/> as monthly averages. The OSNAP AMOC estimate is again defined as the maximum in the overturning stream function computed from a combination of AVISO altimetry data with EN4 temperature and salinity data. Data were provided by Stuart Cunningham (SAMS) as monthly averages.

2.3.2 North Atlantic Oscillation (NAO)

The NAO is the surface atmospheric pressure difference between the Icelandic Low and Azores High. Here, we use the index defined as the normalised pressure difference between Gibraltar and southwest Iceland (Jones *et al.*, 1997). Data were downloaded from the Climatic Research Unit (<https://crudata.uea.ac.uk/cru/data/nao/>) and the winter (DJFM) mean calculated.

2.3.3 Atlantic Multi-decadal Oscillation

We use an AMO index created by averaging SST from the 5°x5° Kaplan dataset over 0-70 °N before de-trending using a 10 year running mean (Enfield *et al.*, 2001). This was downloaded from the National Oceanic and Atmospheric Administration (<https://www.esrl.noaa.gov/psd/data/time-series/AMO/>) as monthly averages.

2.3.4 Strength of subpolar gyre (SPG)

We define the strength of the SPG using the commonly used first principal component associated with the sea surface height field over the subpolar North Atlantic (Häkkinen and Rhines, 2004; Hátún *et al.*, 2005). A version calculated from altimetry data between 40-65 °N and 60 °W-10 °E was downloaded from <https://data.marine.gov.scot/dataset/sub-polar-gyre-index>. This compares well to previous iterations (Berx and Payne, 2017) and is available as monthly averages.

3. Results: Long term mean state

3.1 Atlantic-wide

We first consider the long-term mean state and associated variability at the basin-scale by examining Atlantic-wide maps using output from the VIKING20 model (section 3.1.1) and the observational EN4 dataset (Section 3.1.2).

3.1.1 VIKING20

The mean and the variability of each of the core variables from VIKING20 are shown in Figures 2-7. Since the variability of shallower waters can be orders of magnitude larger than the variability of deeper waters, the variability maps are shown on a \log_{10} scale to highlight the variability over the whole domain.

The maps of mean and variability of the core variables are consistent with well-known oceanographic features. A broad list of observations is:

- (1) shallow waters tend to exhibit greater variability than deeper waters (Figures 2-7).
- (2) shallow waters have higher temperatures than deeper waters (Figure 2).
- (3) a salinity maximum can be used as a tracer for spreading of Mediterranean Overflow Water along the eastern boundary of the North Atlantic (Figure 3).
- (4) the subtropical and subpolar gyres exhibit local SSH maxima and minima, respectively and the strongest variability in SSH is a marker of the Gulf Stream and North Atlantic Current (Figure 4).
- (5) the deepest mixed layers occur in the Subpolar Gyre consistent with known regions of deep convection (Figure 6).
- (6) the cyclonic boundary currents of the Subpolar Gyre contain the highest mean KE along the bottom (Figure 7). The highest bottom eddy KE is coincident with both the SPG boundary currents, as well as the deep eddy-driven recirculation gyres that underlie the Gulf Stream and North Atlantic Current (Gary *et al.*, 2011).

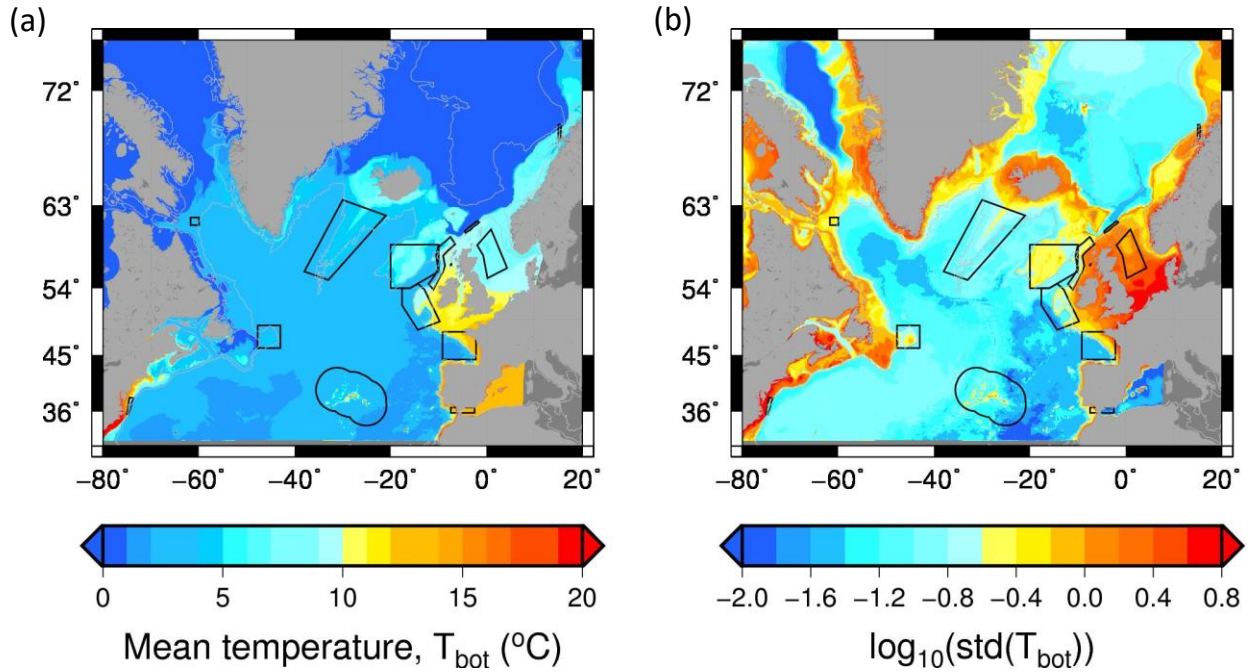


Figure 2. Map of (a) mean and (b) variance of bottom potential temperature, T_{bot} ($^{\circ}\text{C}$) from VIKING20 model output from 1959 to 2009.

Case Studies are shown with the boxes corresponding to Figure 1. The 200m and 2000m isobaths are shown with grey lines. Closed isobath contours with a small number of points are omitted for clarity.

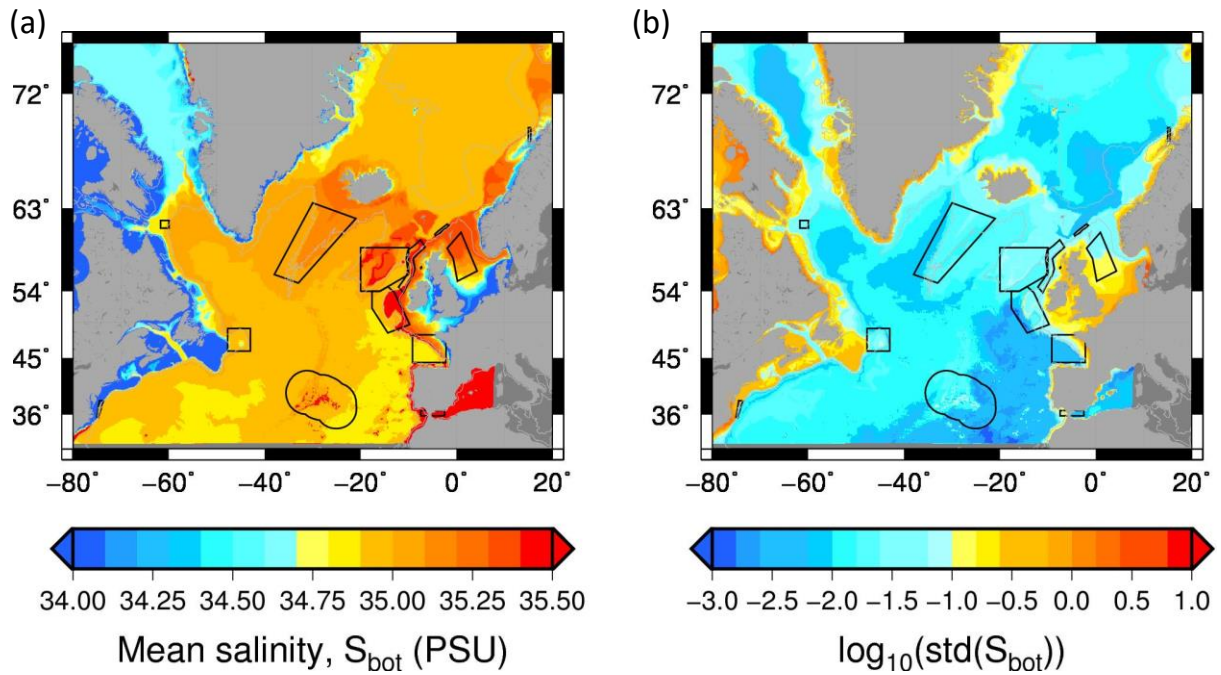


Figure 3. As figure 2 but for bottom salinity, S_{bot} .

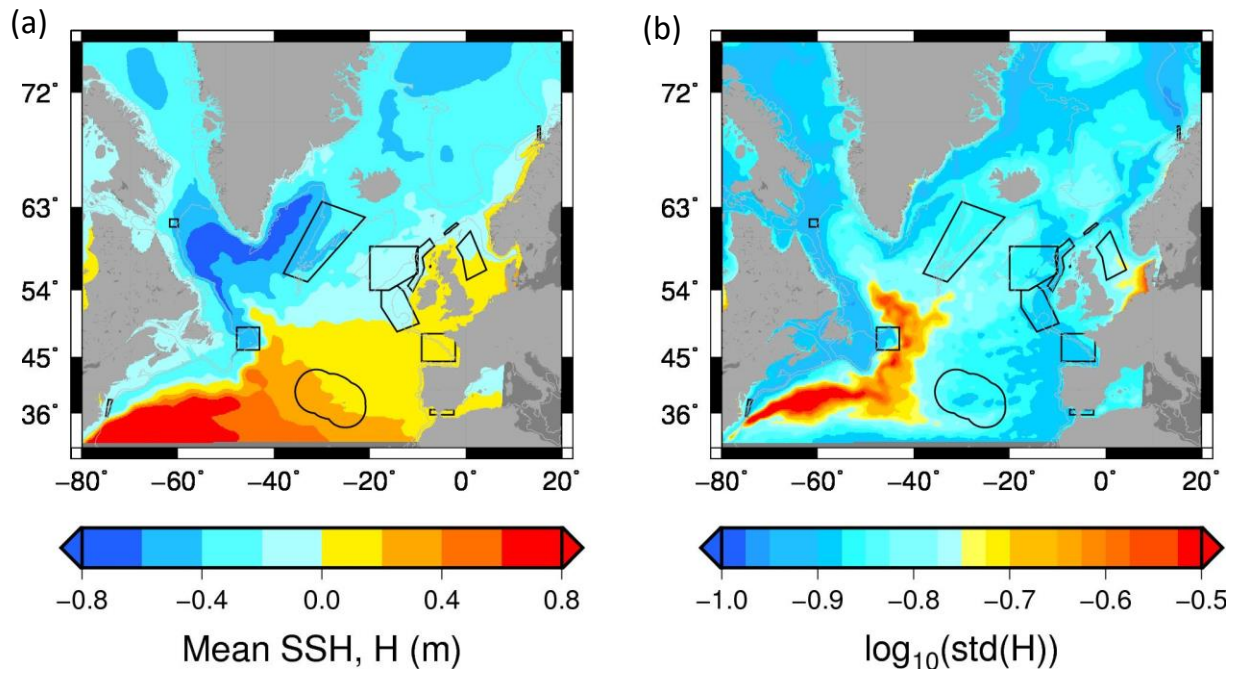


Figure 4. As figure 2 but for sea surface height, SSH (m).

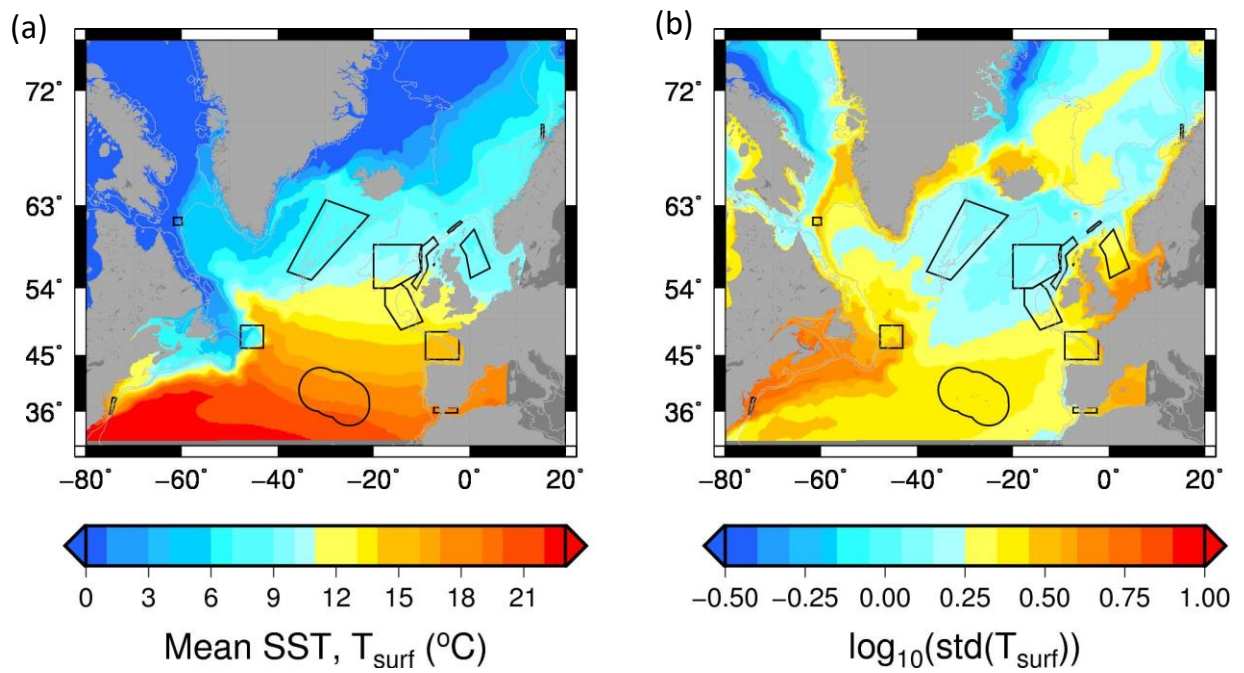


Figure 5. As figure 2 but for sea surface temperature, SST ($^{\circ}\text{C}$).

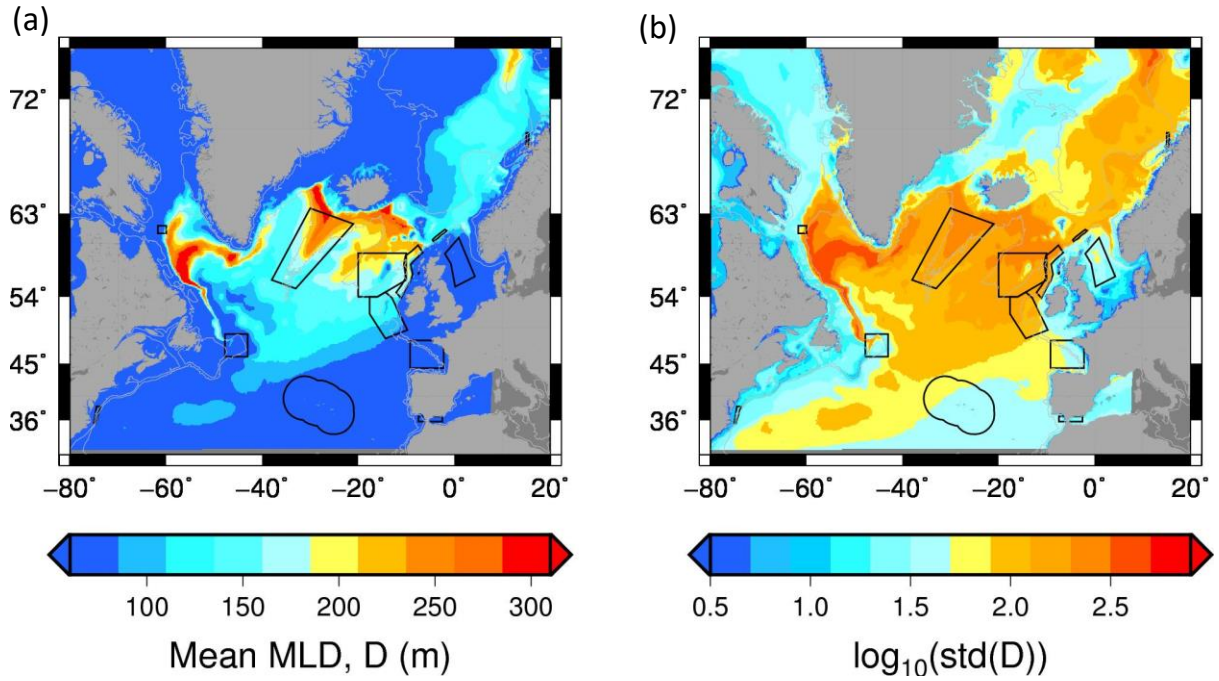


Figure 6. As figure 2 but for mixed layer depth, MLD (m).

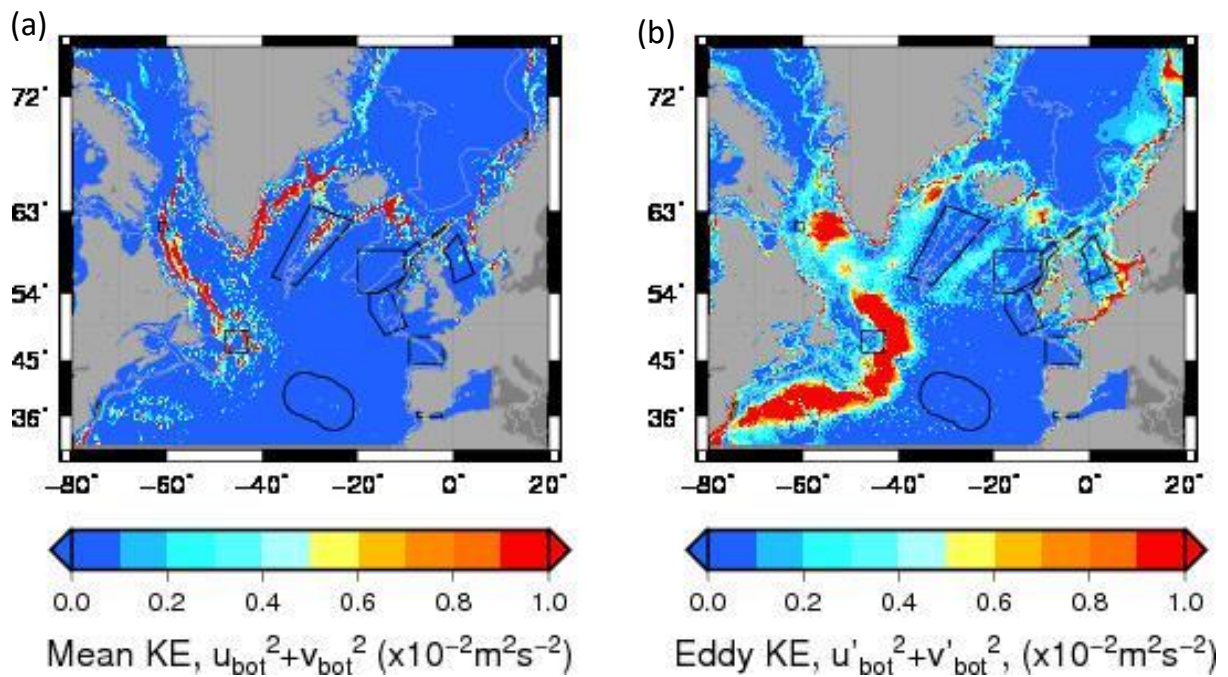


Figure 7. As figure 2 but for bottom kinetic energy, KE_{bot} ($\text{m}^2 \text{s}^{-2}$).

Of particular interest and relevance to ATLAS, we see a local maximum in bottom potential temperature variability that follows the European continental shelf break, roughly bracketed between the 200m and 2000m isobaths and separate from the high variability on the shelf itself (Figure 8). The variability in bottom salinity (Figure 3, no zoom shown) and eddy KE (Figure 9) also exhibit similar local maxima coincident with the shelf break. The local maxima in bottom potential temperature and salinity correspond roughly to the depth range of the main (i.e. non-seasonal) thermocline/halocline/pycnocline in this region, suggesting that this pattern is caused by local vertical heave of the water masses constrained by the steep topography of the eastern boundary of the basin. Furthermore, the co-location of local maxima in bottom potential temperature and salinity variability with bottom eddy KE suggest that these large-scale, open-ocean internal waves are interacting with steeply sloping topography and potentially losing energy to local turbulent dissipation.

One hypothesis for why cold water corals tend to live in specific locations, is that the interaction between the large scale internal waves and steeply sloping topography creates highly localized regions of increased turbulence leading to the resuspension of sediment and thus a more favourable place for the filter-feeding corals to live.

Observations on the Western Scottish Slope in the Faroe-Shetland Channel (CS02) exhibit flow-bathymetry interaction (Hosegood and van Haren, 2004) in a location where cold water corals are known to live. The CS02 polygon in Figure 8 contains some of the highest values of the local maxima in bottom potential temperature and salinity variability and eddy KE along the whole eastern boundary. Also this location in VIKING20 corresponds to a minima of mean KE (Figure 9), suggesting that CS02 may be a particularly good environment for corals due to low mean flow but high variability in the flow.

Finally, it is important to note that although the VIKING20 model does not include any internal tides, which are the most likely phenomenon to have the most persistent and dominant contribution to the forcing of turbulence due to flow-bathymetry interactions, low (temporal) frequency internal waves do exist within VIKING20. Additional forcing due to higher frequency waves (e.g. internal tides) could amplify the patterns seen here.

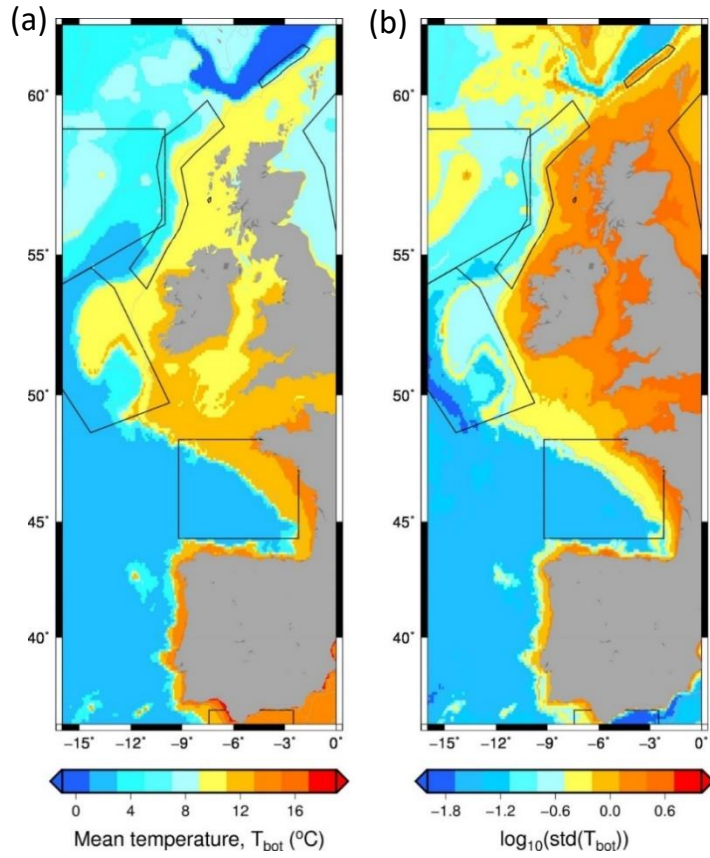


Figure 8. Same as Figure 2 but zoomed in for the subpolar North Atlantic.

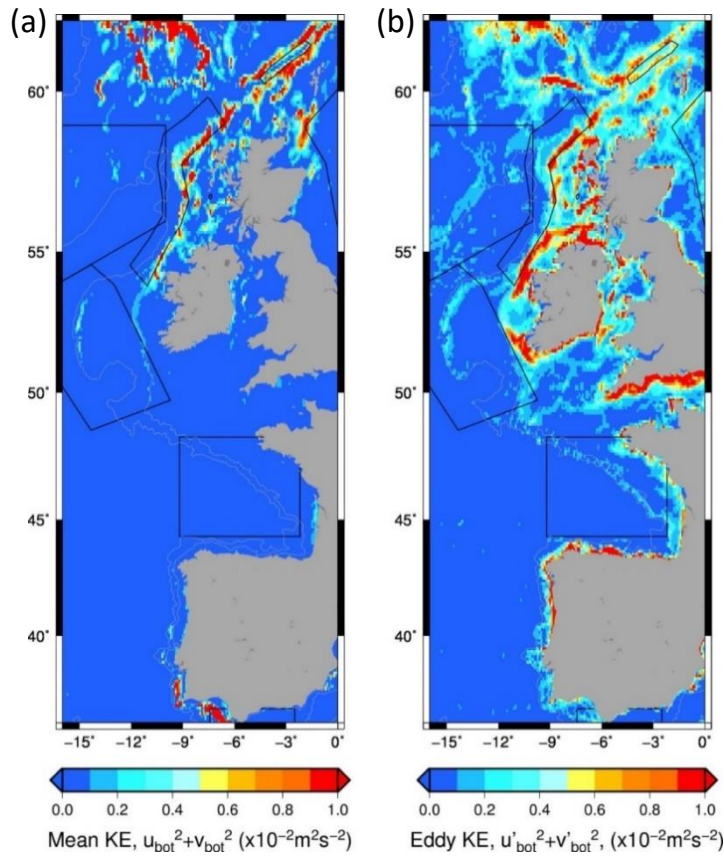


Figure 9. As figure 7 but zoomed in for the eastern subpolar North Atlantic.

3.1.2 EN4

We now present mean and variability maps produced from the observational EN4 dataset, with variability again shown on a logarithmic scale (Figures 10 and 11). It should be noted that this variability is likely to be dominated by seasonal changes. The EN4 and VIKING20 mean maps compare extremely well both in terms of absolute values and spatial patterns. Although there is a slightly different averaging period, 1959-2017 for EN4, and 1959-2009 for VIKING20, this should make little difference.

In respect to bottom potential temperature, both VIKING20 and EN4 show a clear contrast between north and south of the Greenland Scotland Ridge, and south and north of the Davis Strait (Figures 2 and 10). However, bottom potential temperatures in the Atlantic in VIKING20 are slightly warmer than seen in observations. Another difference to note is that the VIKING20 mean shows a lower potential temperature in the very deepest parts of the Atlantic which is not seen in the EN4 dataset. However, the difference between the ocean and shelf areas is captured well. As expected the largest variability in bottom potential temperatures are seen in shallower waters in both VIKING20 and EN4.

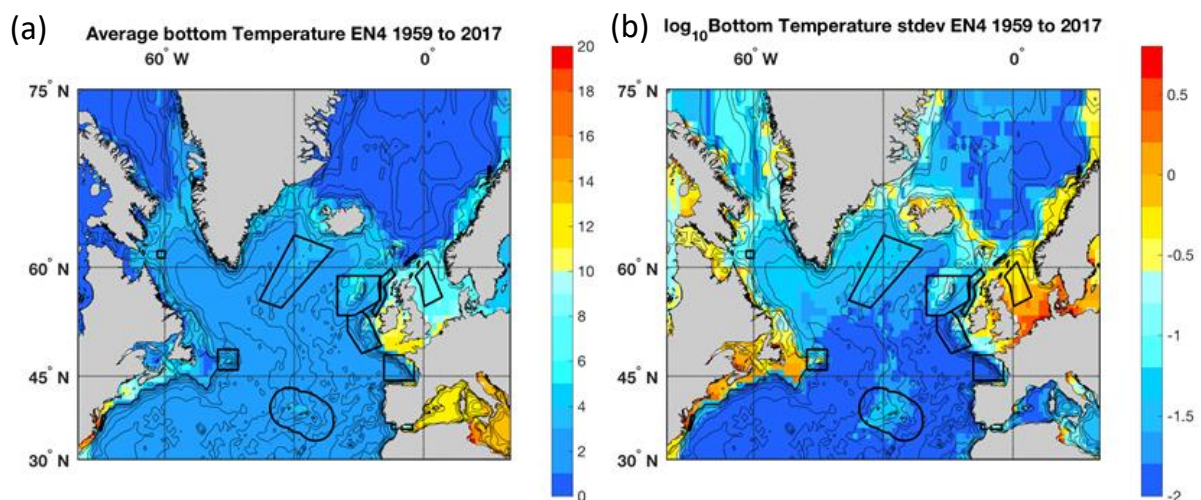


Figure 10. Map of (a) mean and (b) variance of bottom potential temperature, T_{bot} ($^{\circ}\text{C}$) from EN4 observational dataset between 1959 and 2017.

Case Studies are shown with the boxes corresponding to Figure 1.

Mean bottom salinities again compare extremely well between EN4 and VIKING20 with spatial patterns such as differences between shelves and deeper areas represented well (Figures 3 and 11). Interestingly, although the bottom potential temperature in EN4 does not show a difference in the deepest areas of the Atlantic, bottom salinity does show a reduction similar to that observed in VIKING20. Due to the coarser spatial resolution of EN4 (1°) relative to VIKING20 ($1/20^{\circ}$), small

features such as the Azores and some aspects of the Greenland-Scotland Ridge are less well resolved in the observational dataset. However, the similarities between VIKING20 and EN4 give confidence in the model output.

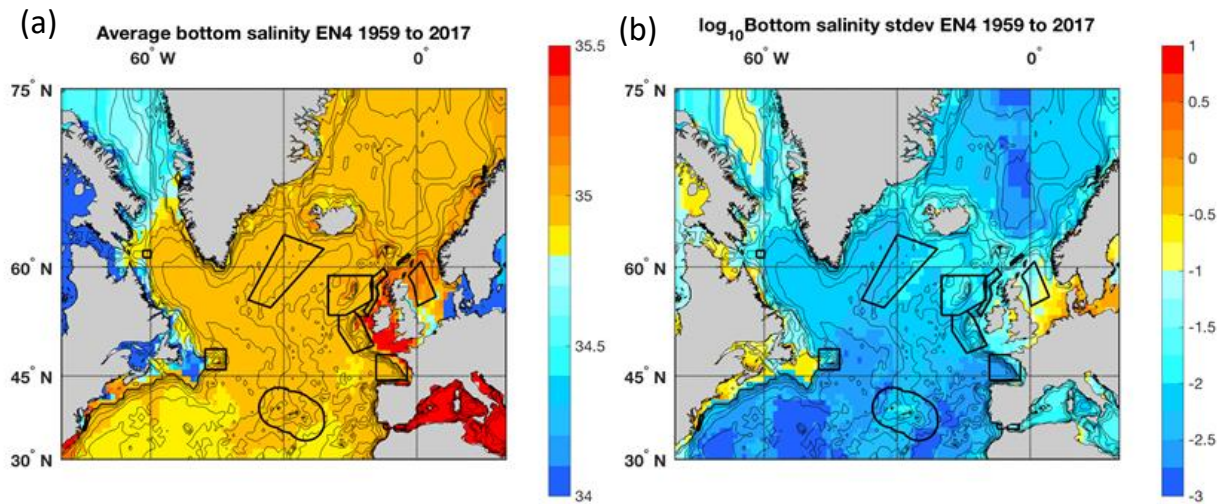


Figure 11. As figure 10 but for bottom salinity, S_{bot} .

3.2 ATLAS case study sites

Having established the long-term mean and associated variability at the basin-scale, we now present averages for each of the case study sites.

3.2.1 VIKING20

The 1959-2009 mean and associated standard deviation, and minimum and maximum values for each case study site are given in Table 2. These were calculated using the 5 day averages and therefore the minimum and maximum values most likely reflect variability at intra-annual timescales.

3.2.2 EN4

The 1959-2017 mean and associated standard deviation, and minimum, and maximum values calculated from EN4 for each case study site are given in Table 3. All case study sites have a mean weighting exceeding 0.05 for both bottom potential temperature and bottom salinity.

Table 2. Long-term mean and associated standard deviation, minimum and maximum for each case study site from VIKING20 5day averages (1959-2009).

	MLD (m)	SST (°C)	T _{bot} (°C)	S _{bot}	KE _{bot} (10 ⁻² m ² s ⁻²)
	mean ± std	mean ± std	mean ± std	mean ± std	mean ± std
	(min / max)	(min / max)	(min / max)	(min / max)	(min / max)
CS01	53 ± 40 (5 / 221)	5.6 ± 1.3 (3.0 / 9.0)	3.2 ± 0.8 (1.6 / 4.9)	27.85 ± 0.09 (27.55 / 28.04)	1.4 ± 1.4 (0.0 / 12.2)
CS02	130 ± 109 (6 / 446)	9.5 ± 1.2 (6.9 / 13.1)	3.7 ± 0.7 (1.7 / 6.0)	35.14 ± 0.04 (35.02 / 35.28)	1.1 ± 0.4 (0.2 / 4.0)
CS03	171 ± 166 (6 / 597)	10.4 ± 1.3 (8.5 / 13.9)	5.8 ± 0.1 (5.3 / 6.0)	35.19 ± 0.02 (35.15 / 35.22)	0.1 ± 0.0 (0.0 / 0.3)
CS04	69 ± 44 (6 / 149)	10.2 ± 2.2 (6.1 / 14.9)	9.1 ± 1.5 (5.7 / 13.1)	35.12 ± 0.14 (34.43 / 35.38)	0.5 ± 0.6 (0.0 / 5.7)
CS05	117 ± 114 (6 / 463)	12.2 ± 1.7 (9.8 / 16.6)	5.7 ± 0.1 (5.4 / 5.9)	35.21 ± 0.01 (35.18 / 35.23)	0.1 ± 0.0 (0.0 / 0.2)
CS06	54 ± 42 (6 / 160)	13.8 ± 2.3 (10.1 / 19.4)	5.5 ± 0.2 (4.9 / 6.0)	33.24 ± 0.04 (33.12 / 33.34)	0.1 ± 0.0 (0.0 / 0.6)
CS07	30 ± 21 (6 / 79)	15.8 ± 2.2 (11.8 / 20.3)	11.6 ± 0.2 (11.1 / 12.0)	32.09 ± 0.03 (31.99 / 32.21)	2.7 ± 0.4 (1.5 / 4.7)
CS08	56 ± 45 (6 / 191)	18.5 ± 2.6 (14.8 / 24.5)	3.2 ± 0.0 (3.1 / 3.2)	34.92 ± 0.01 (34.90 / 34.91)	0.0 ± 0.0 (0.0 / 0.1)
CS09	190 ± 164 (6 / 585)	8.1 ± 1.4 (6.7 / 11.3)	4.1 ± 0.1 (3.9 / 4.3)	35.10 ± 0.01 (35.08 / 35.12)	0.4 ± 0.1 (0.2 / 0.7)
CS10	70 ± 88 (6 / 594)	1.7 ± 2.5 (-1.9 / 6.5)	2.8 ± 0.3 (1.8 / 3.7)	34.89 ± 0.03 (34.81 / 35.02)	2.1 ± 0.8 (0.2 / 5.2)
CS11	42 ± 36 (6 / 254)	8.0 ± 2.6 (2.3 / 14.6)	3.5 ± 0.2 (3.0 / 3.9)	34.95 ± 0.02 (34.88 / 35.02)	1.5 ± 0.4 (0.6 / 3.9)
CS12	17 ± 13 (6 / 73)	14.6 ± 5.4 (5.4 / 25.5)	6.0 ± 1.0 (4.2 / 10.0)	34.30 ± 0.20 (33.68 / 34.87)	0.5 ± 0.5 (0.0 / 7.4)
CS13	167 ± 157 (6 / 653)	10.8 ± 1.4 (8.6 / 14.4)	6.8 ± 0.2 (6.3 / 7.4)	35.25 ± 0.02 (35.19 / 35.30)	0.4 ± 0.3 (0.0 / 2.9)
CS14	57 ± 36 (6 / 96)	9.1 ± 2.3 (5.1 / 15.4)	7.9 ± 1.4 (5.1 / 11.2)	35.18 ± 0.07 (34.98 / 35.36)	0.3 ± 0.2 (0.0 / 1.9)

Table 3. Long-term mean and associated standard deviation, minimum and maximum for each case study site from EN4 data (1959-2017).

	T_{bot} (°C)	S_{bot}
	mean ± std	mean ± std
	(min / max)	(min / max)
CS01	-1.0 ± 0.0 (-1.1 / -0.9)	34.91 ± 0.01 (34.88 / 34.95)
CS02	-0.8 ± 0.1 (-1.1 / -0.4)	34.91 ± 0.02 (34.85 / 34.98)
CS03	3.6 ± 0.1 (3.5 / 3.8)	34.97 ± 0.01 (34.93 / 35.02)
CS04	9.5 ± 0.4 (8.2 / 11.1)	35.38 ± 0.03 (35.25 / 35.46)
CS05	3.6 ± 0.0 (3.5 / 3.8)	35.01 ± 0.01 (34.98 / 35.03)
CS06	4.4 ± 0.1 (4.1 / 4.6)	35.06 ± 0.01 (35.02 / 35.10)
CS07	9.4 ± 0.2 (8.9 / 10.1)	36.00 ± 0.07 (35.77 / 36.20)
CS08	2.4 ± 0.0 (2.4 / 2.5)	34.93 ± 0.01 (34.91 / 34.95)
CS09	2.9 ± 0.1 (2.7 / 3.1)	34.95 ± 0.01 (34.92 / 34.99)
CS10	3.2 ± 0.1 (3.0 / 3.5)	34.91 ± 0.02 (34.88 / 35.00)
CS11	2.5 ± 0.1 (2.2 / 2.7)	34.91 ± 0.01 (34.88 / 34.96)
CS12	3.0 ± 0.1 (2.8 / 3.11)	34.96 ± 0.01 (34.91 / 35.00)
CS13	4.0 ± 0.1 (3.7 / 4.2)	35.00 ± 0.02 (34.92 / 35.06)
CS14	7.6 ± 0.7 (5.9 / 9.4)	35.17 ± 0.07 (34.84 / 35.41)

4. Results: Seasonal variability

Having established the long-term mean, we now investigate the seasonal cycle at each case study site by calculating monthly anomalies before fitting a sine curve to the resulting values (e.g. figure 12). Any curves with a period less than 10 months, or more than 14 months, were considered not to be representative of the seasonal signal and were discounted from further analysis. A further step discounted any seasonal cycles with an amplitude less than the expected instrumental measurement accuracy (i.e. 0.01 for temperature and 0.001 for salinity). Again, we carry out the analysis using both output from the VIKING20 model (section 4.1) and the observational EN4 dataset (section 4.2).

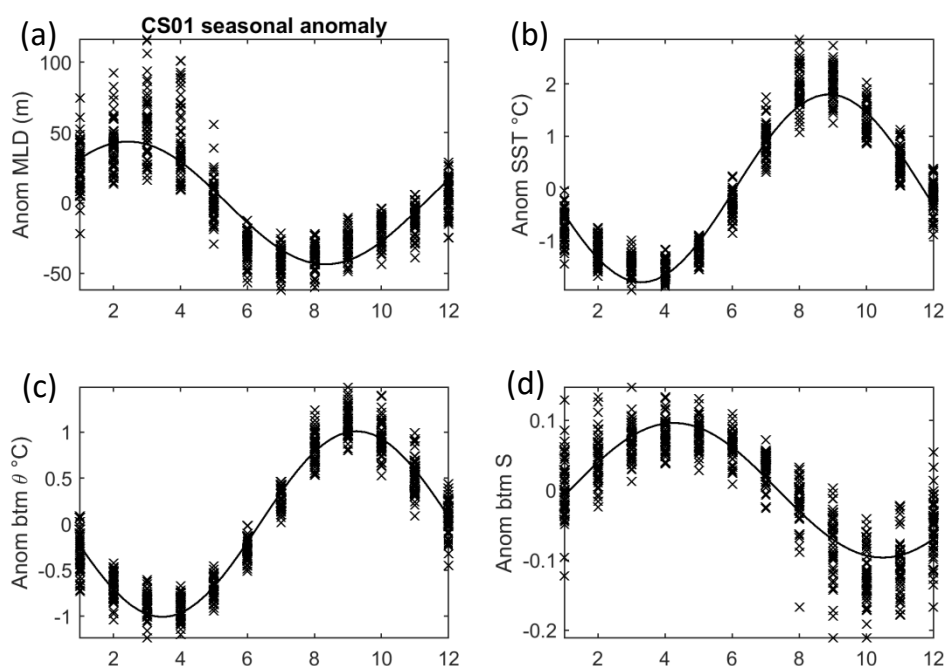


Figure 12. Example of the method used for the calculation of seasonal cycle phases and amplitudes at case study sites.

Monthly anomalies of (a) MLD, (b) SST, (c) bottom potential temperature and (d) bottom salinity (crosses) plotted against month. Line shows fitted sine curve.

4.1 VIKING20

Mixed layer depth shows a pronounced seasonality with the maximum depths reached between January and March (Figure 13). As expected the largest seasonal signal is seen in the subpolar areas with reduced convection depths south of 50 °N (Table 4).

Table 4. Amplitude (and phase) of the seasonal cycle in VIKING20 from 1959-2009.

A phase of 0 represents a maximum in March and a minimum in September, whilst a phase of -3 represents a maximum in December and a minimum in June, and a phase of +3 represents a maximum in June and a minimum in December. Dashes indicate where a seasonal cycle could not be established.

	MLD (m)	SST (°C)	T_{bot} (°C)	S_{bot}
	amplitude (phase)	amplitude (phase)	amplitude (phase)	amplitude (phase)
CS01	44 (-1)	1.8 (-5)	1.0 (-5)	0.10 (+1)
CS02	138 (-2)	1.6 (-5)	0.5 (-2)	0.02 (-0)
CS03	202 (-1)	1.8 (-5)	0.0 (-5)	-
CS04	48 (-2)	3.0 (-6)	1.8 (-6)	0.04 (-3)
CS05	134 (-1)	2.3 (-6)	0.1 (-4)	0.01 (-4)
CS06	54 (-2)	3.2 (-6)	0.2 (-6)	0.04 (-7)
CS07	27 (-2)	3.0 (-6)	0.1 (-7)	0.02 (-1)
CS08	58 (-2)	3.5 (-5)	-	-
CS09	207 (-1)	1.7 (-5)	0.0 (+3)	-
CS10	72 (-3)	3.1 (-5)	0.2 (+0)	0.02 (+1)
CS11	41 (-2)	3.4 (-6)	-	0.01 (+5)
CS12	15 (-3)	7.3 (-6)	0.8 (-6)	0.08 (-5)
CS13	192 (-1)	1.9 (-5)	0.2 (-5)	-
CS14	47 (-1)	3.2 (-6)	1.8 (-6)	0.02 (-0)

As expected the seasonal cycle in SST has a maximum in October and minimum in April (Figure 14 and Table 4). The amplitude is higher at coastal sites and at the more southerly case study sites with CS12 having the largest seasonal variability. In contrast, amplitudes are lowest at the offshore subpolar case study sites (CS02, CS03, CS09 and CS13) as well as at the LoVe Observatory (CS01).

The seasonal cycle for bottom potential temperatures is much smaller than for SST (Figure 15 and Table 4). There is no discernible seasonal cycle in bottom potential temperatures at CS08 and CS11 and only small seasonal cycles (less than or equal to 0.2 C) at other case study sites away from the boundaries of the Atlantic Ocean. The largest seasonal cycle (1.8 C) is observed at CS04 on the Scottish Shelf and CS14 in the North Sea. The phase of the seasonal cycle (if present) is roughly in phase with the seasonal cycle in SST with the exception of CS09 and CS10. CS09 shows a maximum in

June and minimum in December whilst CS10 shows a maximum in March and a minimum in September.

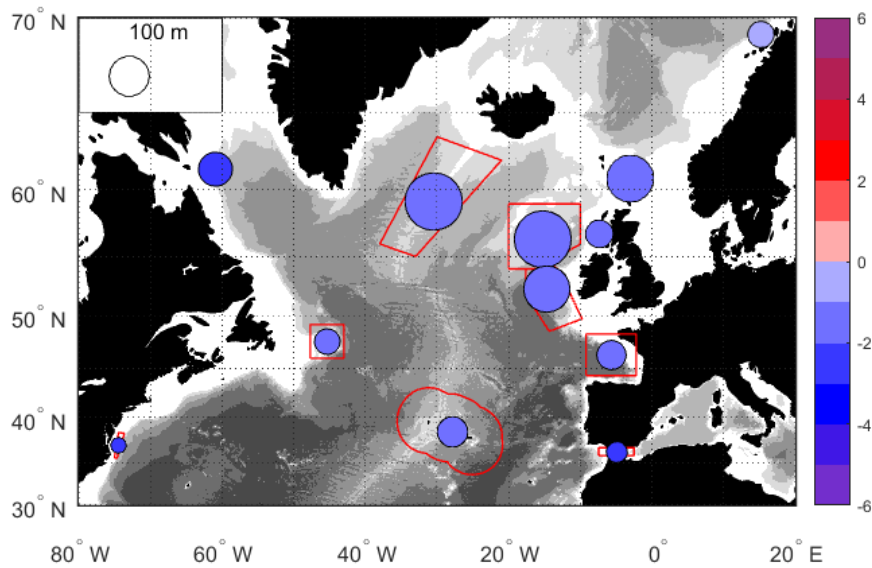


Figure 13. Seasonal cycle associated with mixed layer depth, MLD (m) between 1959 and 2009 in VIKING20 at case study sites. Circle size represents the amplitude of the seasonal cycle, and colour the phase. A phase of 0 represents a maximum in March and a minimum in September, whilst a phase of -3 represents a maximum in December and a minimum in June, and a phase of +3 represents a maximum in June and a minimum in December.

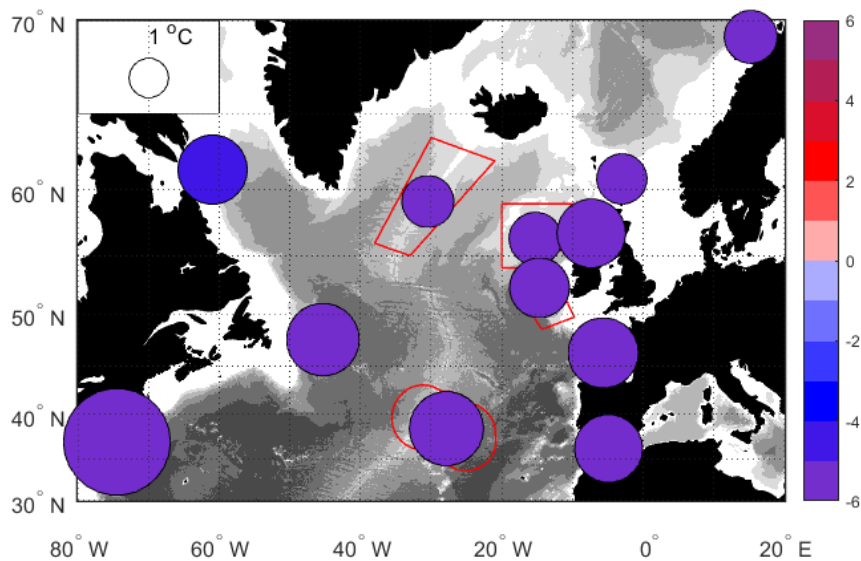


Figure 14. As figure 13 but for sea surface temperature, SST (°C).

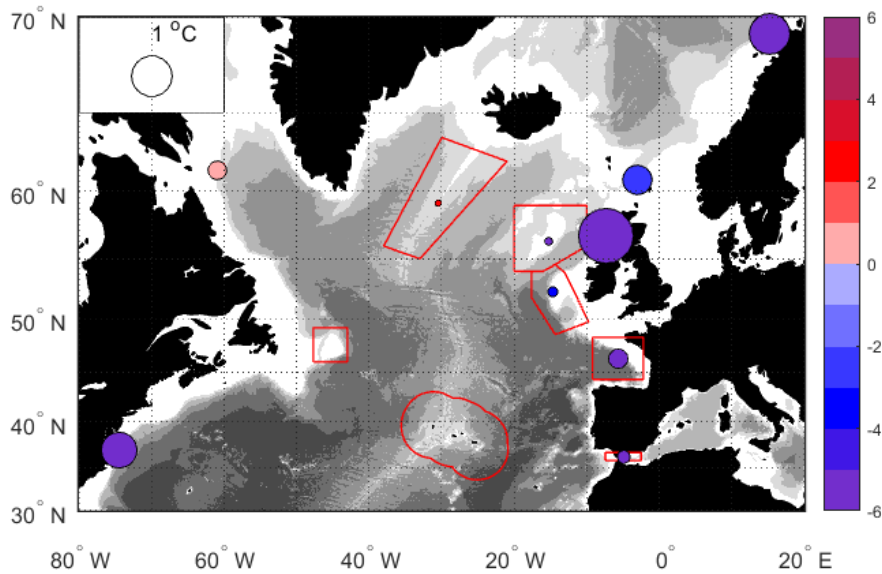


Figure 15. As figure 13 but for bottom potential temperature, T_{bot} ($^{\circ}\text{C}$).

For bottom salinity the picture is more varied (Figure 16 and Table 4). Five case study sites have no discernible seasonal cycle, whilst CS01 and CS12 have the largest seasonal cycle with an amplitude of 0.1 and 0.08 respectively. The phase is also much more variable between sites. Whereas CS02, CS05, CS06, CS10 and CS12 have similar phases for both bottom potential temperature and salinity, other case studies are six months out of phase between the two variables. For these sites (CS01, CS07 and CS14) the warmest bottom temperatures are associated with the freshest bottom conditions and vice versa.

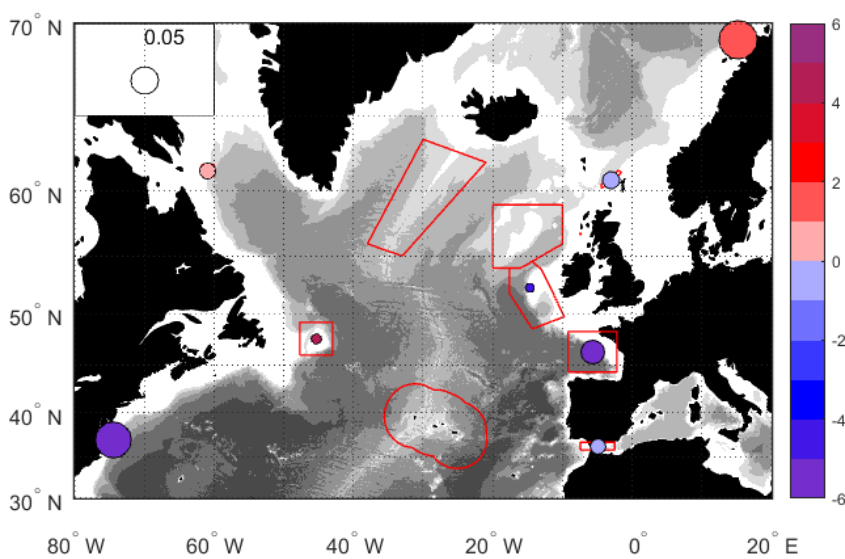


Figure 16. As figure 13 but for bottom salinity, S_{bot} .

Seasonal analysis is best suited to properties rather than energy, thus we do not apply the method to KE_{bot} . However, there is some evidence (not shown) of reduced variability in bottom kinetic energy in the summer months relative to the winter.

4.2 EN4

The amplitude of the seasonal cycle is smaller in the observational dataset compared to VIKING20 for both bottom potential temperature and bottom salinity (Table 5, Figures 17-18). For bottom potential temperature, no discernible seasonal cycle is observed at CS03, CS08 and CS11, whilst CS04 has a clear cycle (amplitude 0.3 °C) but with a period of 14.1 months. The case studies along the eastern boundary (CS02, CS05, CS06, CS07) have a phase of ranging from -4 to -6 indicating a maximum between September and November (Figure 17). In contrast, the case studies on the western boundary (CS10 and CS12) have a phase of -1, which indicates maximum values in February and minimum temperatures in August.

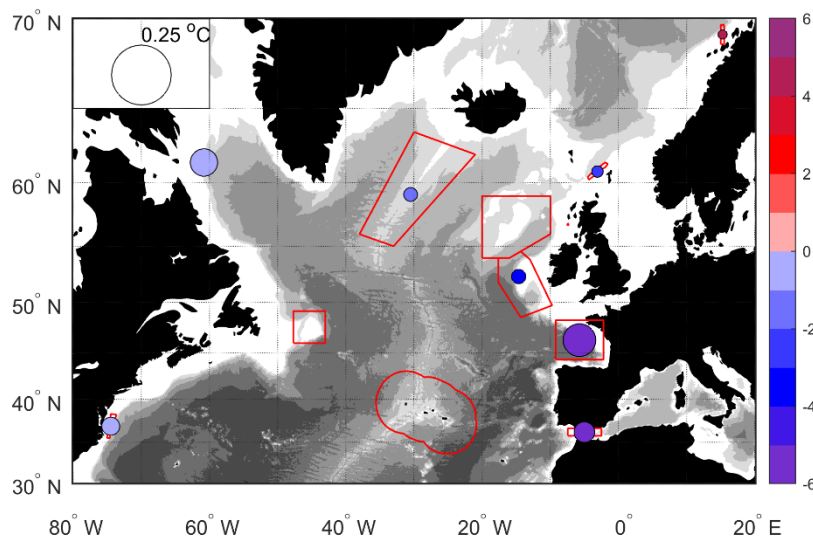


Figure 17. Seasonal cycle associated with bottom potential temperature (°C) between 1959 and 2017 in EN4 at case study sites. Circle size represents the amplitude of the seasonal cycle, and colour the phase. A phase of 0 represents a maximum in March and a minimum in September, whilst a phase of -3 represents a maximum in December and a minimum in June, and a phase of +3 represents a maximum in June and a minimum in December.

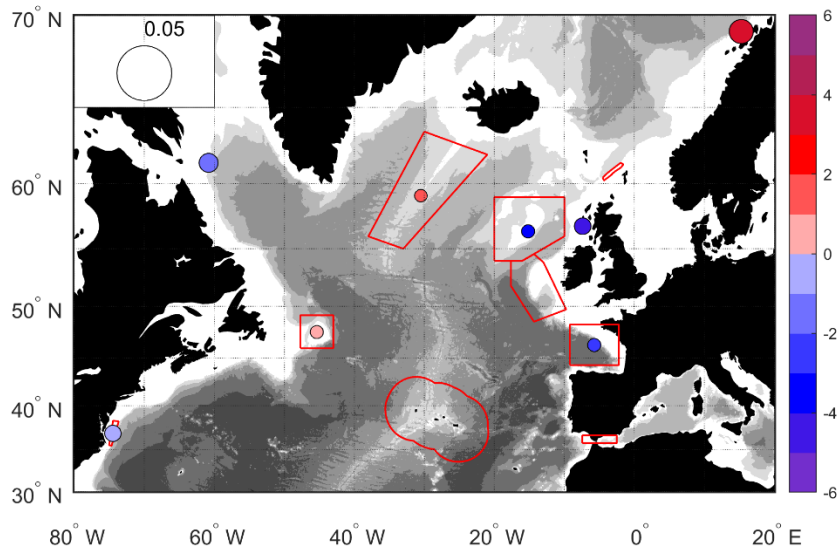


Figure 18. As for figure 17, but for bottom salinity.

Table 5. Amplitude (and phase) of the seasonal cycle in EN4 from 1959-2017.

A phase of 0 represents a maximum in March and a minimum in September, whilst a phase of -3 represents a maximum in December and a minimum in June, and a phase of +3 represents a maximum in June and a minimum in December. Dashes indicate sites where a seasonal cycle could not be established.

	T_{bot} (°C)	S_{bot}
	amplitude (phase)	amplitude (phase)
CS01	0.01 (+4)	0.010 (+3)
CS02	0.01 (-2)	-
CS03	-	0.003 (-3)
CS04	-	0.005 (-5)
CS05	0.01 (-4)	-
CS06	0.08 (-6)	0.003 (-3)
CS07	0.03 (0)	-
CS08	-	-
CS09	0.01 (-2)	0.003 (+2)
CS10	0.05 (-1)	0.006 (-2)
CS11	-	0.003 (0)
CS12	0.02 (-1)	0.005 (0)
CS13	0.02 (-1)	0.010 (-4)
CS14	0.74 (-5)	0.043 (+2)

For bottom salinity, no discernible seasonal cycles is seen at four case studies (CS02, CS05, CS07 and CS08). The phase of the seasonal cycle ranges from -3 to -5 in the eastern boundary of the North Atlantic, representing a maximum in October to December, and a minimum from April to June. However, CS01 at LoVE Observatory on the Norwegian Coast, has a phase of +3 for bottom salinity and +4 for bottom potential temperature. Thus, at this location a maximum in bottom temperature and salinity is observed in June-July, with minimum values seen in December-January.

5. Temporal variability of climate indices

Having established the long-term mean and the size of the seasonal cycle, we now move on to investigating four climate indices that effect the North Atlantic region: the AMO, AMOC, SPG and NAO. Time series of these indices are shown in Figures 19 and 20. For the AMO, AMOC, and SPG we show monthly averages, smoothed annual averages (running mean with gaussian filter), and five year smoothed time series. For the NAO, the data are presented as DJFM means and five year smoothed data.

We define high (low) states of each climate index as greater (less) than one standard deviation from the mean of the time series respectively. Histograms of high and low timestamps for the monthly averaged time series show a seasonal bias for the AMOC and AMO indices (Figures A1-A5). The high AMOC periods within the VIKING20 time series are primarily associated with the Spring and Autumn months, whilst low AMOC states are associated with the winter months. Likewise, the high periods in the OVIDE AMOC time series are biased towards the spring and the low periods towards the later half of the year. A weakened but similarly distributed signal is seen for the high periods in the AMOC time series derived across the OSNAP section. The AMO time series also shows a slight seasonal bias for the high states towards the summer months. In contrast the SPG index does not show any seasonal bias.

Whilst the seasonality persists in some of the indices despite annual smoothing, the signal is removed for all indices once the time series is smoothed at a five-year temporal resolution (Figures A1-A5). As any seasonal bias makes it difficult to distinguish between the seasonal signal and any changes related to the climate indices, we now focus on the five year smoothed time series. Again, we define high and low states of each climate index as greater or less than one standard deviation from the mean of the time series respectively (dashed lines, Figure 19).

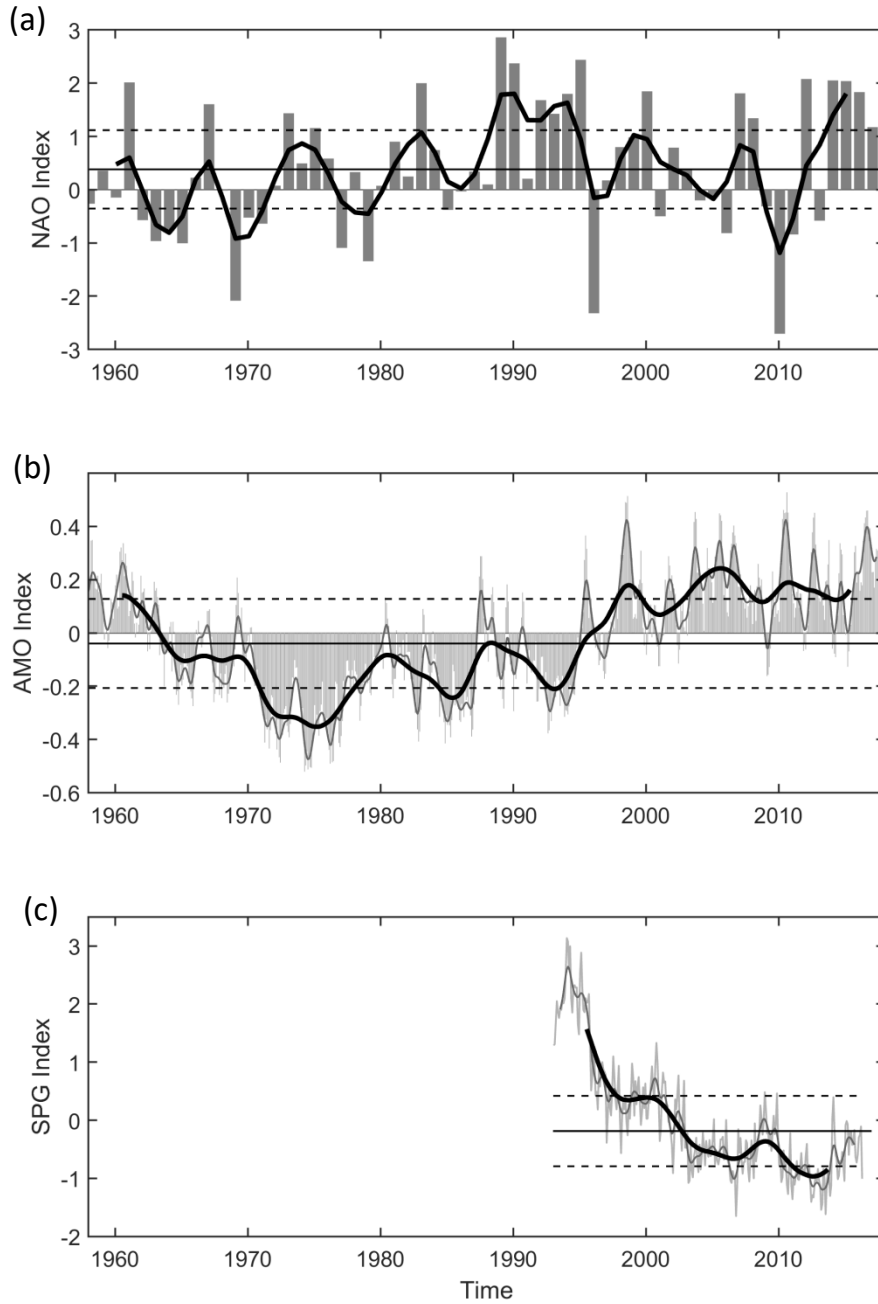


Figure 19. Time series of climate modes which affect the North Atlantic: (a) NAO index, (b) AMO index, and (c) SPG index.

(a) bars show mean DJFM index and thick black line 5yr smoothed time series. (b) Light grey bars show monthly means, grey line annually-smoothed time series and thick black line 5yr smoothed time series. (c) Light grey line shows monthly averages, grey line annually-smoothed time series and thick black line 5yr smoothed time series. (a-c) Thin black and dashed lines show mean plus and one standard deviation variability for each 5yr smoothed time series. Time series were smoothed using a running mean with a gaussian filter.

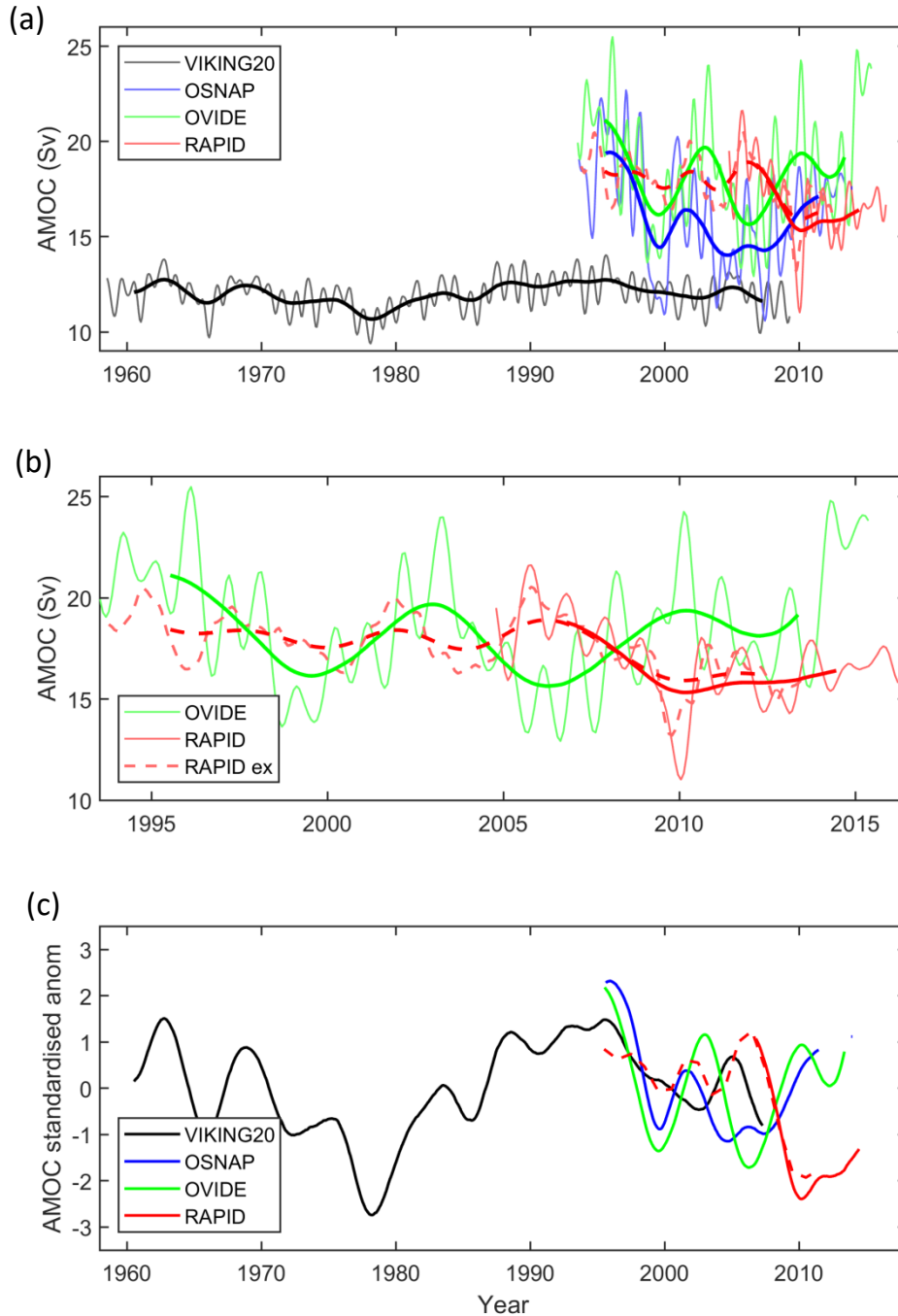


Figure 20. Time series of AMOC variability: (a) comparison of observed time series (OVIDE: green, OSNAP: blue, RAPID: red) with time series extracted from VIKING20 (black); (b) comparison of OSNAP and RAPID time series; (c) standardised anomalies of 5yr smoothed observed and modelled time series.

(a and b) faded lines show annually-smoothed time series and solid lines 5yr smoothed time series. Red dashed line shows the RAPID time series extension of Frajka-Williams (2015). Time series were smoothed using a running mean with a gaussian filter. Note the different x-axis on (b).

For the NAO (Figure 19.a), high states are seen in the early 1990s and since 2015, and low states in the early 1960s, around 1970 and around 2010. The AMO (Figure 19.b) shows a longer periodicity than the NAO. A low state was seen in the 1970s with the index being in a high state from the late 1990s to present. The record for the SPG index is much shorter, beginning in 1993. In general a weakening is observed between 1993 and the present with a small increase in the late 2000's (Figure 19.c). We note that the SPG and AMO indices appear similar. Although the SPG index is only a 14 year record, a further investigation such as a comparison between the modelled SPG index (e.g. Hátún *et al.*, 2005) and the AMO over a longer time period may be interesting.

For the AMOC time series, we first note that the VIKING20 time series has a lower mean and variability than the observed time series (Figure 20.a). The observational time series agree well with some suggestion that the RAPID and OVIDE time series may, at times, be out of phase (Figure 20.b). In order to better compare the VIKING20 and observational time series, we compute standardised anomalies by subtracting the mean for each time series and dividing by the standard deviation (Figure 20.c). The AMOC time series calculated along the OSNAP and OVIDE time series compare well, especially at the start and end of the record. The VIKING20 time series appears to be intermediate to the subpolar and subtropical time series which is not surprising considering that it is a latitudinal average between approximately 35 and 60 °N. The mean meridional variability associated with the averaged AMOC in VIKING20 is ~ 4 Sv. For simplification from here on, we limit analysis to the VIKING20 and OVIDE versions of the AMOC.

6. Results: Spatial variability linked to AMOC states

We now search for relationships between large-scale climate indices and water properties across the North Atlantic using the composite method (Duchez *et al.*, 2016). This involves averaging time stamps which are above (below) one standard deviation from the mean to create high (low) composites. In this section we investigate the signature of the AMOC creating maps for the high and low AMOC states using both VIKING20 and EN4.

As the AMOC is derived from oceanic variables, and changes in the modelled and real-world ocean may not be contemporaneous, we use the modelled AMOC time series to examine changes in VIKING20 and an observational time series to examine effects in the EN4 dataset. For VIKING20, anomalies representing the high and low states were calculated by subtracting the mean over all time steps from the selectively averaged maps. This process was done with the high and low time

periods for both the raw time series (i.e. 5 day averages) and 10 year smoothed time series to highlight the impacts of the AMOC seasonal cycle and decadal variability respectively. To create the composites for the EN4 dataset, we opt to use the observational AMOC index calculated along the OVIDE section. Additionally, due to the relatively short nature of the observational record (<15 years), we use a five year smoothing to look at longer term variability, rather than the 10 year smoothing used for the VIKING20 output.

6.1 VIKING20

On seasonal or decadal time scales the relationship between the AMOC and bottom potential temperature is strongest in the shallow shelf waters with comparatively weaker signals in the deep ocean (Figure 21). On a seasonal time scale, the shelf waters unsurprisingly reflect the fact that the AMOC is weakest (strongest) and temperatures are coolest (warmest) in the winter (summer). On the decadal timescale, this pattern is reversed along the continental shelf of the western boundary with the strongest association with the low (high) AMOC being the warmer (cooler) waters, especially near CS12. The decadal scale relationship between the AMOC and bottom potential temperature along the western boundary is also reflected in bottom salinity with warmer, saltier waters on the western shelf and colder, fresher waters on the eastern shelf during low AMOC states (Figure 22). During high AMOC states, there are fresher, colder waters on the western shelf.

In contrast to bottom temperature and salinity, whose variability is primarily on the basin edge, the relationship between SSH and AMOC exhibits a strong signal in the basin interior. The seasonal pattern for SSH reflects primarily the seasonal steric rise and fall of SSH as the seasonally heated upper layer warms and cools (Figure 23). On decadal time scales, there is a meridional gradient in SSH anomalies such that the Subtropical Gyre is lower than the Subpolar Gyre during low AMOC states (positive gradient). The gradient reverses during high AMOC states. This pattern is broadly consistent with the rise and fall of the subpolar gyre relative to the subtropical gyre used on decadal time scales as a large-scale index representing the flow in the North Atlantic (Curry and McCartney, 2001) that has also been shown to be consistent with the strength of the North Atlantic Current in models (Scheinert, 2008) and the Deep Western Boundary Current (Böning *et al.*, 2006), two major constituents of the AMOC.

Similarly to SSH, the seasonal pattern in SST primarily reflects seasonal cooling in winter, synchronous with the lower AMOC and the summer warming, also synchronous with the higher AMOC (Figure 24). However, while SSH shows a change in meridional gradient on decadal time

scales, SST shows very little consistent change in the Subpolar Gyre while there are substantial changes in the Subtropical Gyre. A possible explanation for this is that subtropical surface waters are not directly exported into the Subpolar Gyre, rather it is likely that the surface waters of the Subpolar Gyre must first sink into the underlying mode waters before being exported to the Subpolar Gyre (Burkholder and Lozier, 2014; Burkholder and Lozier, 2011) so it is unlikely that there is a direct surface pathway for surface temperature anomalies between the two Gyres (Foukal and Lozier, 2016).

Mixed layer depth follows a strong seasonal cycle due to deep convection brought about by winter storms. Since the AMOC is also weakest in the winter, deeper MLD associated with weaker AMOC is no surprise. However, on the decadal timescale, an inverted pattern appears so deeper convection is synchronous with a stronger AMOC (Figure 25). The correlation between deep convection in the Subpolar Gyre and AMOC is a known feature in VIKING20 and many other models but, as yet, is not directly verified by observations (Lozier *et al.*, 2016).

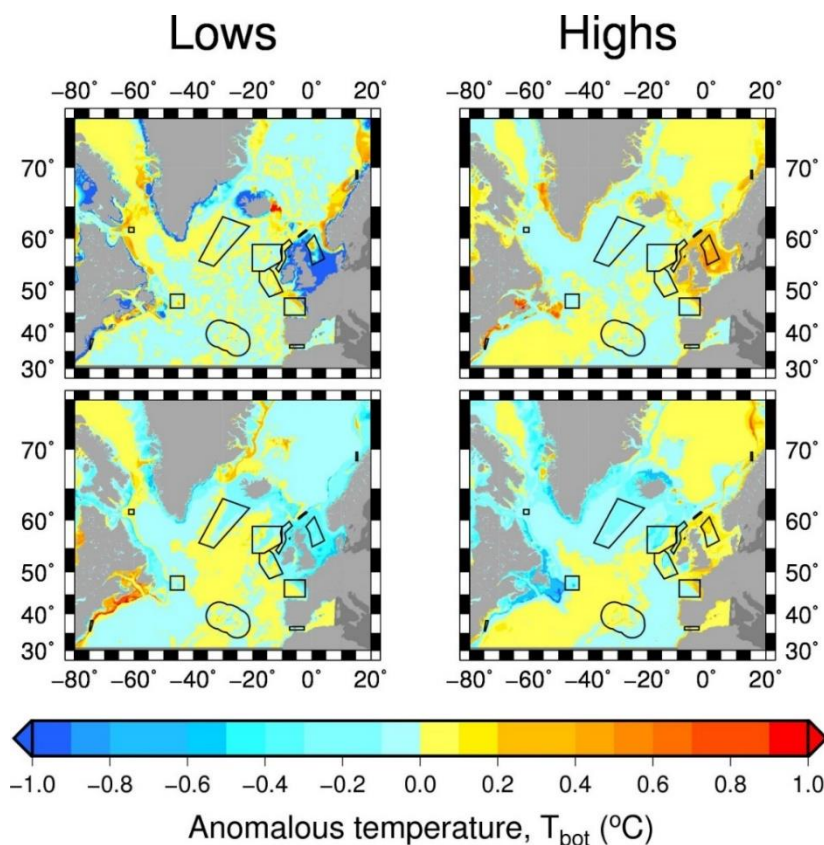


Figure 21. Anomalies of VIKING20 bottom potential temperatures, T_{bot} ($^{\circ}\text{C}$) averaged over high and low states of the AMOC derived from VIKING20.

The top row corresponds to high and low values of the 5 day averaged AMOC time series, whilst the bottom row corresponds to high and low values associated with the 10 year smoothed time series.

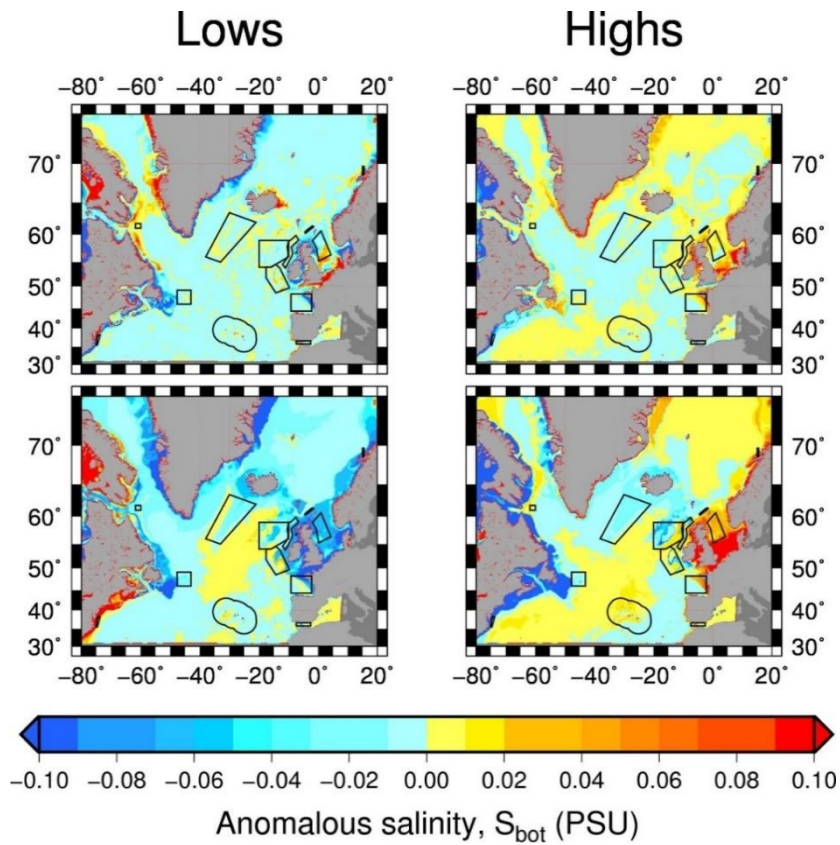


Figure 22. As figure 21 but for bottom salinity, S_{bot} .

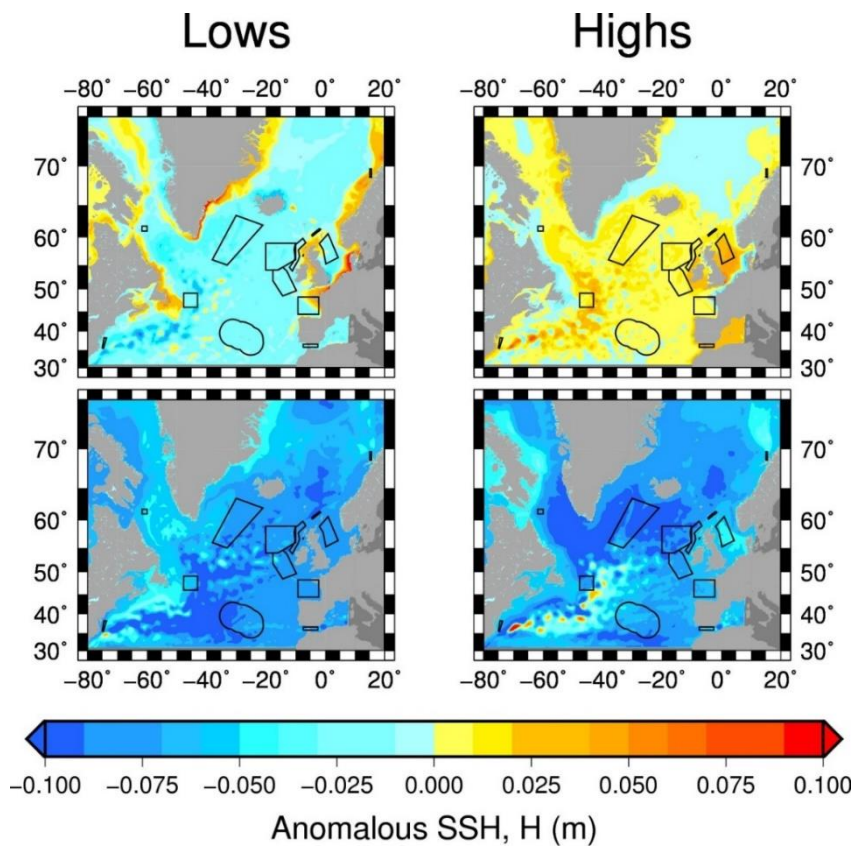


Figure 23. As figure 21 but for sea surface height, SSH (m).

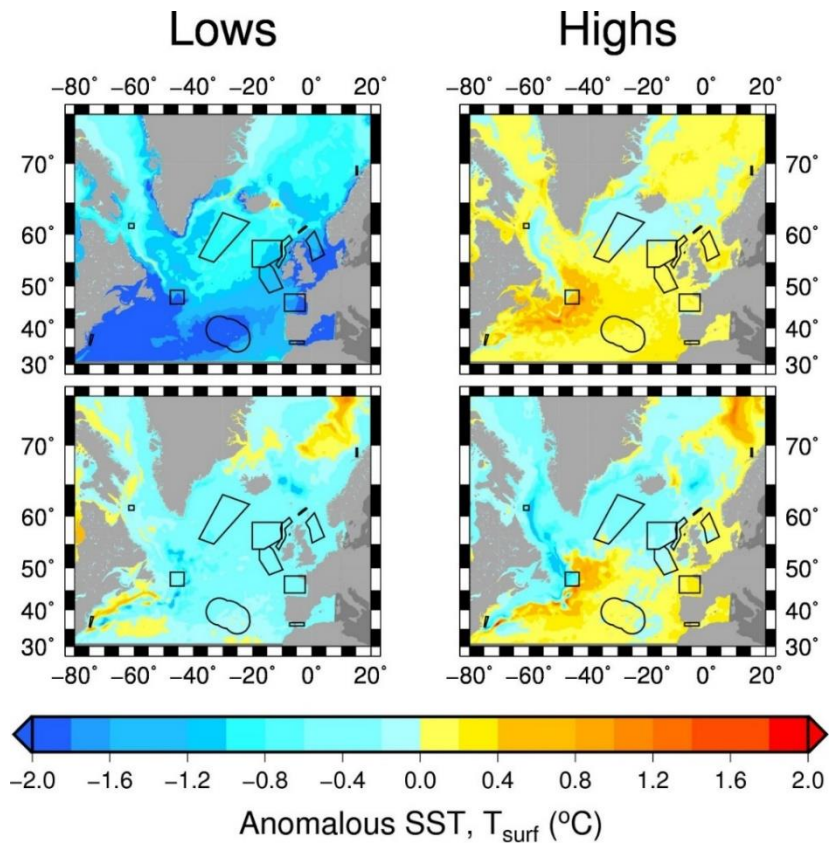


Figure 24. As figure 21 but for sea surface temperature, SST (°C).

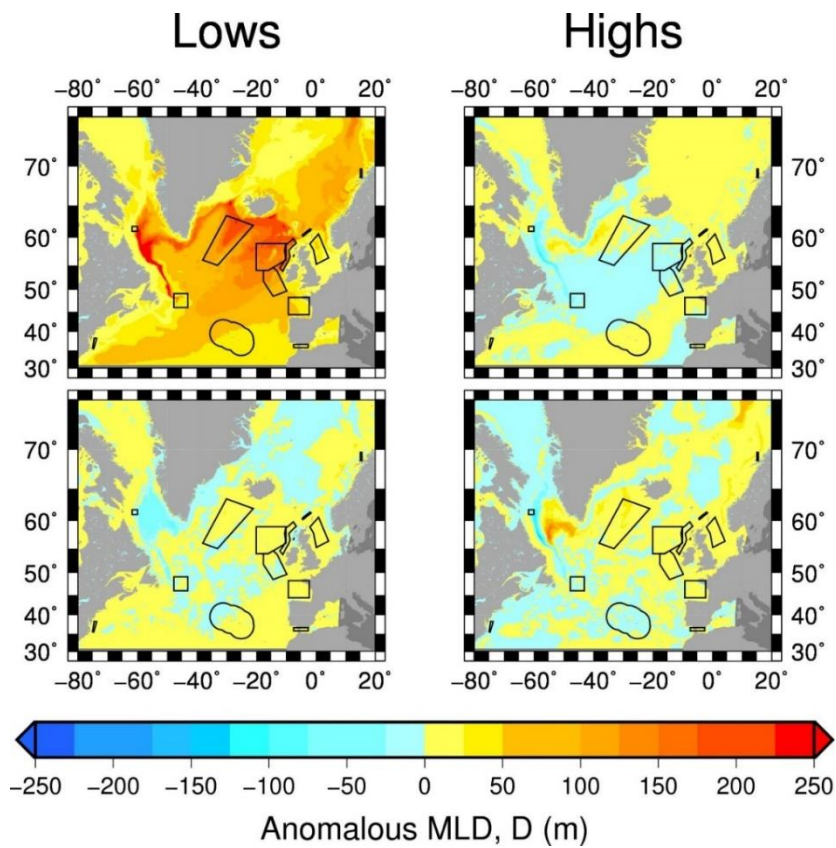


Figure 25. As figure 21 but for mixed layer depth, MLD (m).

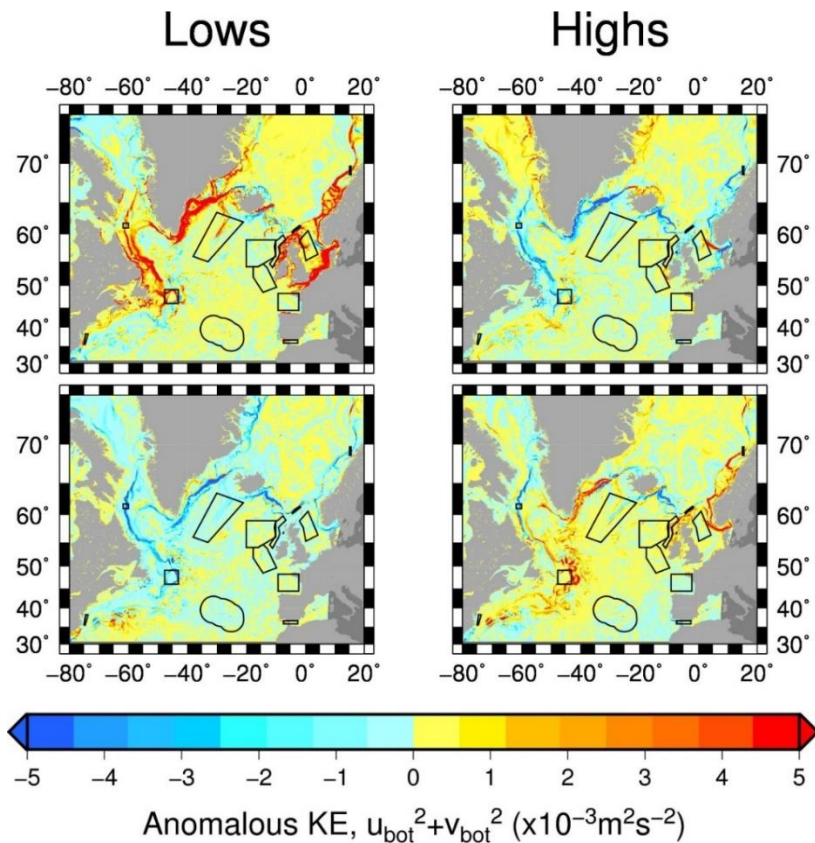


Figure 26. As figure 21 but for bottom kinetic energy, KE_{bot} (m^2s^{-2}).

As with AMOC and MLD, relationship between AMOC and kinetic energy shows an inversion between the spatial patterns at seasonal and decadal timescale. On the seasonal timescale, the wintertime forcing spins up the boundary currents of the Subpolar Gyre during low AMOC states while the Subpolar Gyre boundary currents slow-down in summer during high AMOC states (Figure 26). In contrast to the seasonal time scale, on decadal timescales, stronger boundary current circulation is associated with stronger AMOC and vice versa. As the boundary currents are viewed as important components of the subpolar AMOC (Lozier *et al.*, 2016), this relationship is expected. However, the decadal signal in VIKING20 is at best on par or weaker than the seasonal cycle which is consistent with the finding that it is very difficult to detect long term changes in observations of the boundary current (Fischer *et al.*, 2010).

6.2 EN4

Despite the slightly different AMOC index and smoothing period, there are some similarities in the high and low composite maps created from the EN4 dataset and VIKING20. In terms of bottom potential temperature, both EN4 and VIKING20 show lower values around Greenland and the boundaries of the Labrador Sea during high AMOC states (Figure 27.a). A similar signal is seen

immediately north of Iceland. Strong changes are also seen in both datasets around Newfoundland, on the European Shelf and on the southern Norwegian Slope. The EN4 dataset appears to partially resolve the warmer temperatures in the northwest Atlantic south of around 55 °N; however, due to the lack of data in this region (Figure 27.b) we are sceptical of this signal. The EN4 dataset does not show the high bottom potential temperatures in the Nordic Seas that are observed in VIKING20 during a high AMOC state. This again may be due to reduced data coverage in the observational dataset.

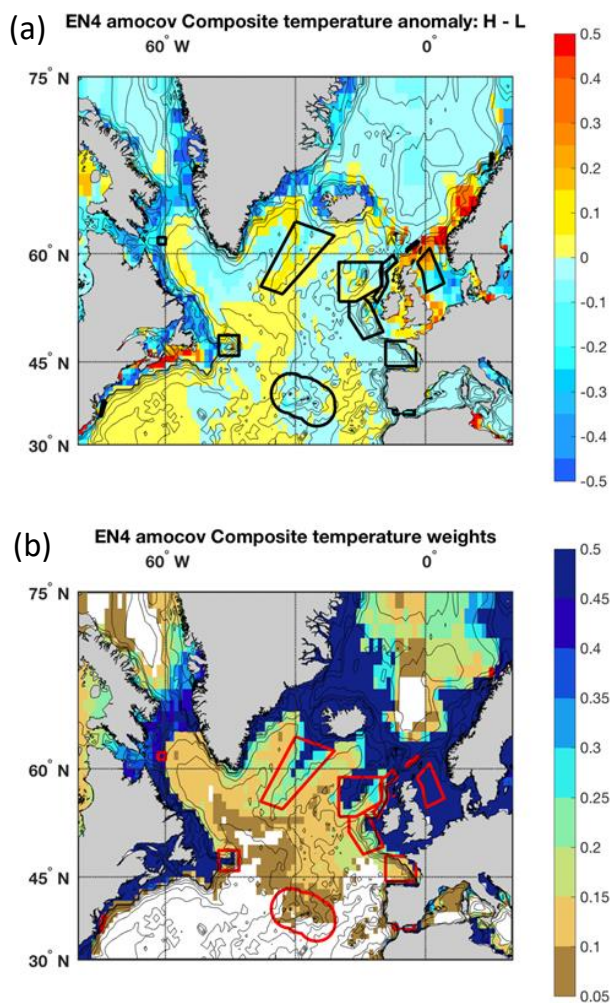


Figure 27. (a) AMOC High minus Low map of bottom potential temperatures, T_{bot} (°C) in EN4 and (b) mean data weighting.

The EN4 data weighting ranges from 0 to 1 with 0 indicating no data availability.

The patterns for bottom salinity are similar. Unsurprisingly the EN4 dataset again does not show the change in salinity observed in VIKING20 for the data sparse Nordic Seas or the abyssal Atlantic south of about 55 °N (Figure 28). There is some suggestion that the bottom salinity composite from EN4

has less features in common with the VIKING20 composites than for bottom potential temperature. In VIKING20 waters on the European Shelf are warmer and saltier during a high AMOC, whilst waters on the western boundary (south of Newfoundland) are cooler and fresher. Although there is some evidence of this in the observations, it is less clear than in the model output.

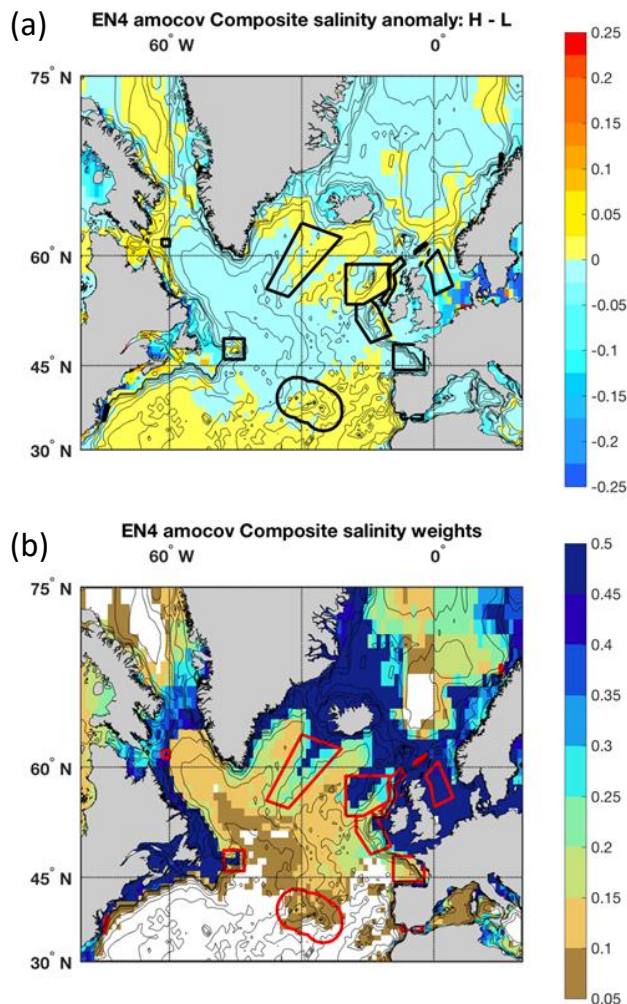


Figure 28. As figure 27 but for bottom salinity, S_{bot} .

7. Results: Spatial variability linked to NAO states

In this section we repeat the analysis of the previous section, but using the winter (DJFM) NAO index. As this is an atmospherically-derived index, and VIKING20 is forced with observational CORE2 atmospheric data, we can use the observational NAO index to produce the composites for both the VIKING20 and EN4 datasets.

7.1 VIKING20

In VIKING20, bottom potential temperature and salinity exhibit an analogous relationship to the NAO (Figures 29 and 30) as they did with the AMOC; both bottom potential temperature and salinity are anti-correlated with the NAO on the western boundary and correlated with the NAO on the eastern boundary. Specifically, low NAO states are associated with warm, salty waters along the Greenland coast, Labrador Shelf, the Grand Banks and as far south as CS12. These same regions along the eastern boundary experience colder, fresher waters during high NAO states. In contrast, on the eastern continental shelf, low NAO states exhibit cold, fresh waters while high NAO states are associated with warmer, saltier waters.

The relationship between SSH and the NAO (Figure 31) is similar to SSH and the AMOC. There is a change in the sign of the gradient of anomalous SSH with a shift in NAO state: a positive gradient is during low NAO states and a negative gradient exists during high NAO states. A stronger negative SSH gradient implies more barotropic mass transport between the two gyres, as noted above. Since the NAO is also essentially a meridional gradient in atmospheric pressure with a strong negative gradient associated with a positive NAO, the anti-correlation between anomalous SSH gradients and the NAO means that anomalous SSH gradients are actually correlated with the atmospheric pressure gradients. This association between SSH (and by extension potential energy anomaly) and the NAO is what motivated the term "oceanic NAO" (Curry and McCartney, 2001).

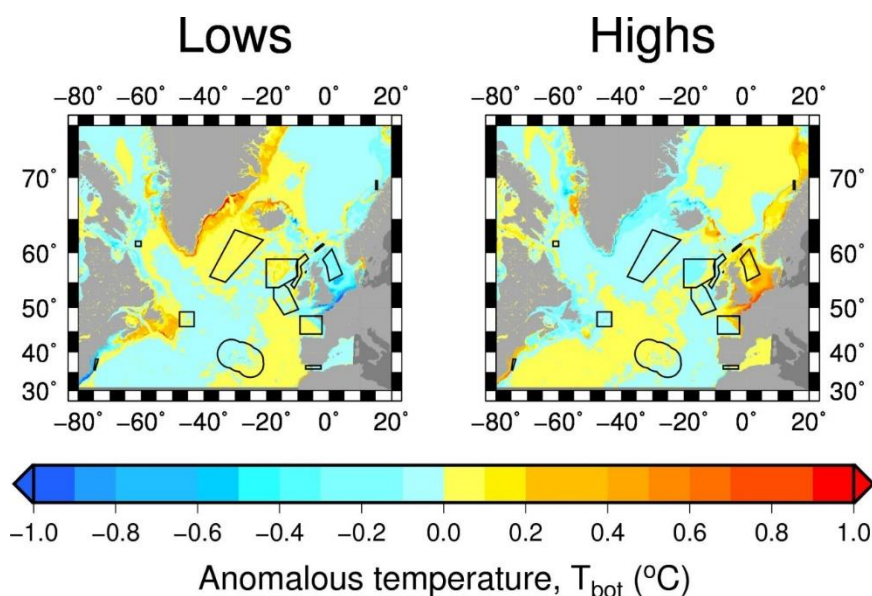


Figure 29. Anomalies of VIKING20 bottom potential temperatures, T_{bot} (°C) averaged over high and low states of the NAO.

Averages were calculated of high and low values of the DJFM averaged NAO time series.

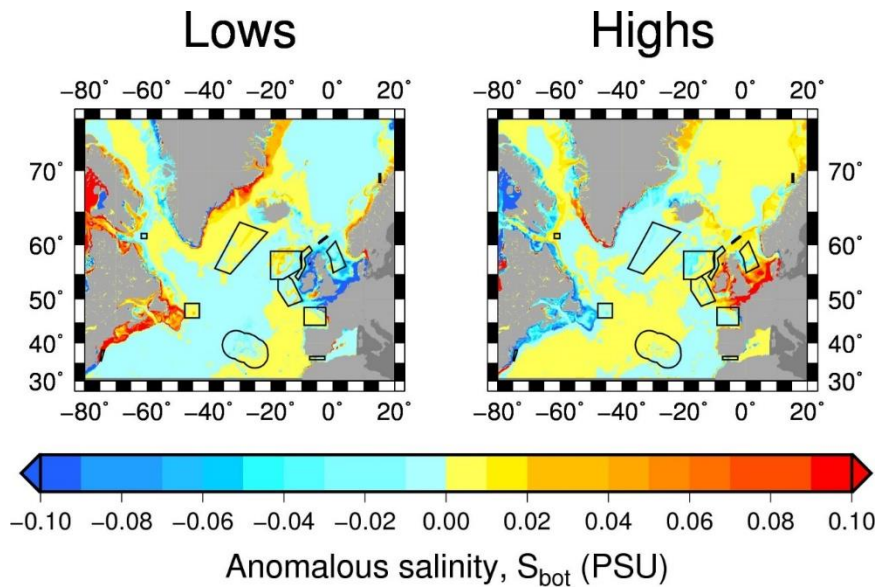


Figure 30. As figure 29 but for bottom salinity, S_{bot} .

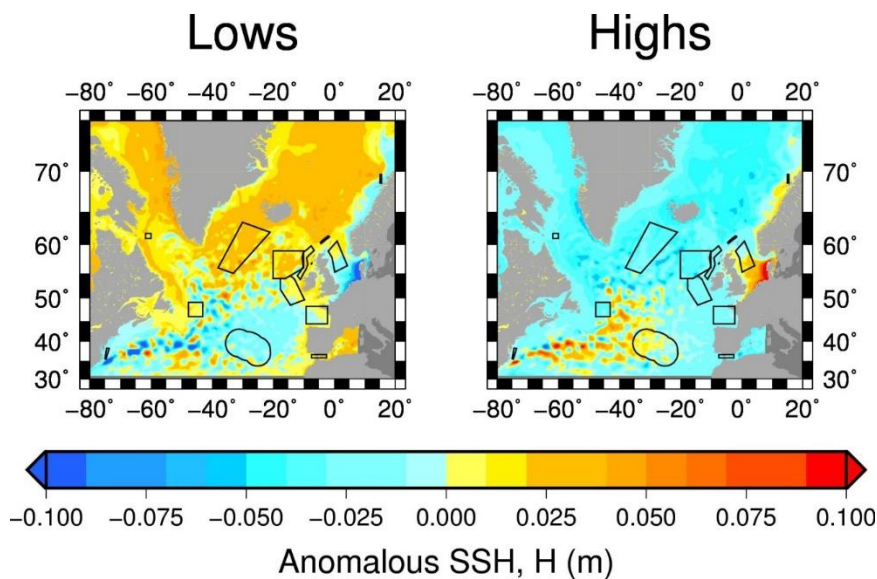


Figure 31. As figure 29 but for sea surface height, SSH (m).

When examining the relationship between the NAO and SST (Figure 32), the more northerly storm track and stronger winters associated with high NAO states tend to cool the surface waters of the SPG during high NAO. Conversely, low NAO states result in a warmer SPG with the more southerly storm track generally causing cooling of the surface waters in the Subtropical Gyre. Another result consistent with the prevailing understanding of the NAO is that stronger winters associated with high NAO states are associated with in deep convection in SPG. The weaker winters associated with low NAO states and a more southerly storm track cause a basin-wide deepening of the MLD in the Subtropical Gyre rather than the highly localized deep convection in Subpolar Gyre.

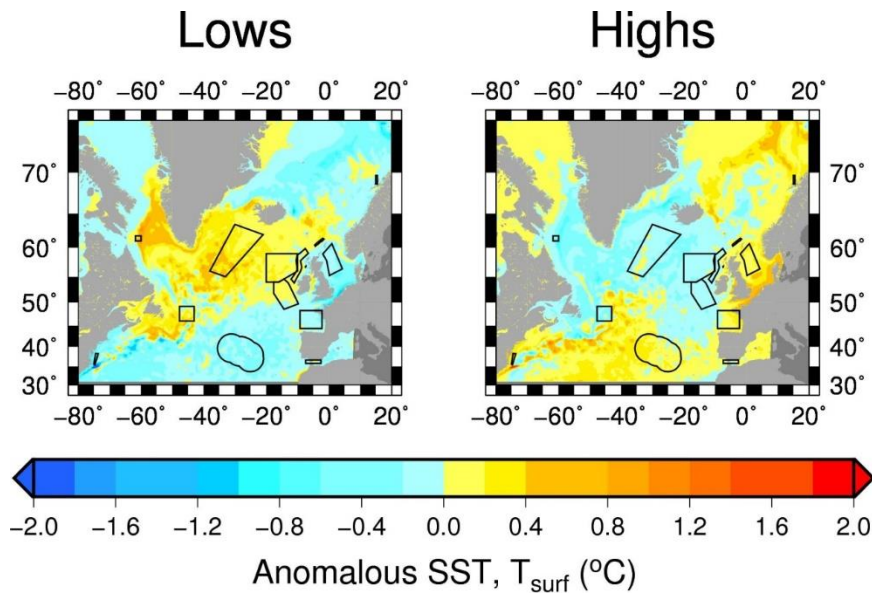


Figure 32. As figure 29 but for sea surface temperature, SST (°C).

In VIKING20, low NAO states are associated with a stronger Deep Western Boundary Current in the Labrador Sea (Figure 33). This negative correlation, which has also been recently observed (Zantopp *et al.*, 2017), also holds for high NAO states which are associated with weaker Deep Western Boundary Current flow. The exact mechanisms underlying this association are yet to be identified. That the East Greenland Current in VIKING20 appears to be correlated with the NAO, while the DWBC appears to be anti-correlated with the NAO presents a compelling dynamical contrast meriting further study.

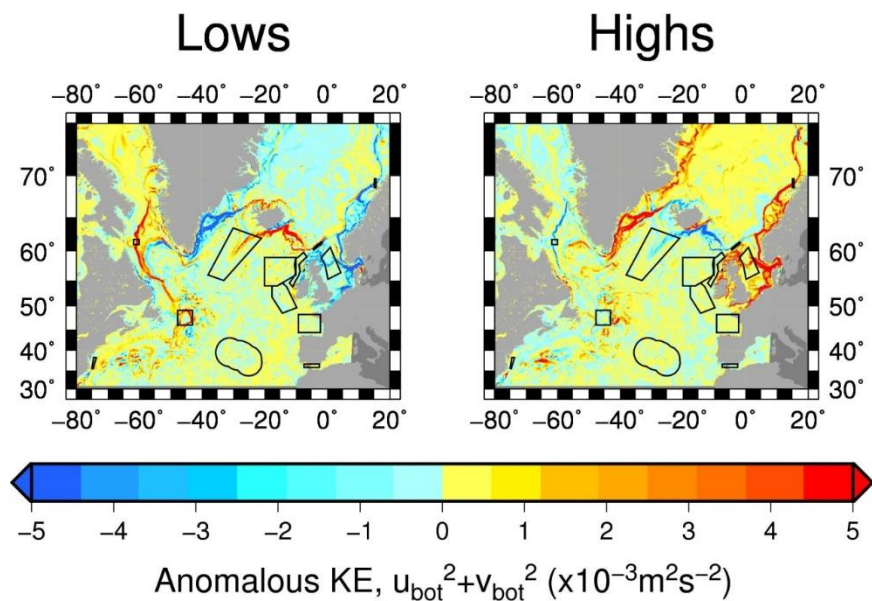


Figure 33. As figure 29 but for bottom kinetic energy, KE_{bot} ($\text{m}^2 \text{s}^{-2}$).

7.2 EN4

We now present the composites produced from the EN4 observational data set. These were created using the five-year smoothed DJFM mean NAO time series and therefore represent longer term variability than investigated using VIKING20. Despite the different smoothing period used, the high minus low maps produced from EN4 for the NAO compare well to output from VIKING20 around the boundaries of the Atlantic Ocean, and less well in the data sparse abyssal areas (Figures 34-35).

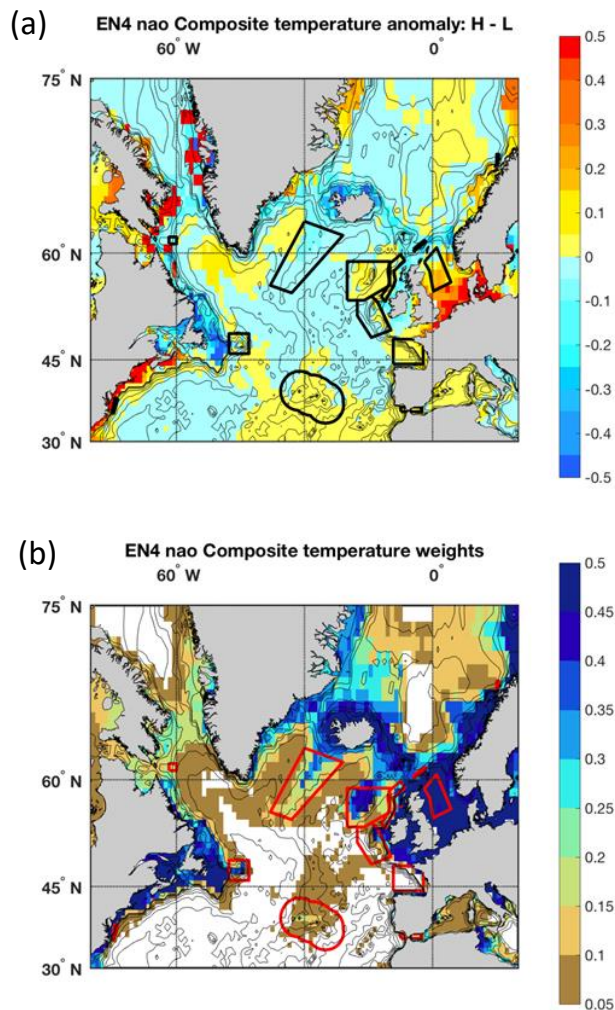


Figure 34. (a) NAO High minus Low map of bottom potential temperatures, T_{bot} (°C) in EN4 and (b) mean data weighting.

The EN4 data weighting ranges from 0 to 1 with 0 indicating no data availability.

In terms of bottom potential temperature, the clear east-west split in the deep Atlantic south of about 55°N in the VIKING20 maps is not observed in the EN4 dataset (Figure 34). Similarly, the warmer conditions in the deep areas of the Nordic Seas during a high NAO, and cooler conditions during a low NAO, seen in VIKING20 are not observed in the EN4 composite. However, the changes

in the North Sea and along the Norwegian coast are resolved well, as are the changes around Iceland and along the east coast of Greenland. The strong signal near Newfoundland and south along the USA coast are also common to both the EN4 and VIKING20 dataset. Finally, some structure around the boundary of the Labrador Sea is also observed in both datasets.

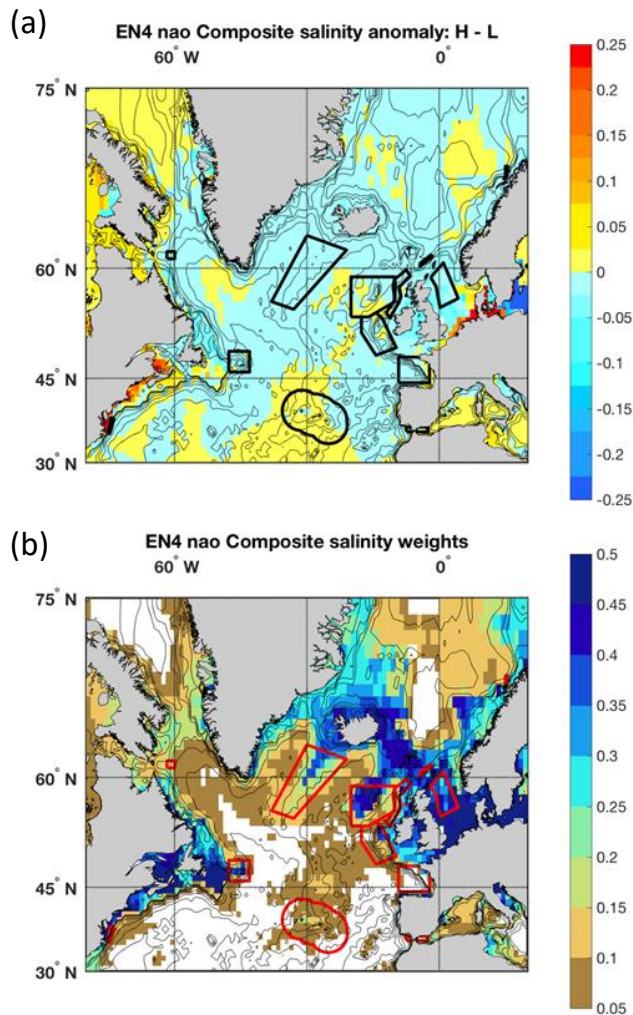


Figure 35. As figure 34 but for bottom salinity, *S_{bot}*.

The EN4 and VIKING20 salinity composites agree less well (Figure 35). As expected the patterns seen in the deeper areas of the Atlantic and Nordic Seas within the VIKING20 composites are not observed in the EN4 dataset. However, some of the features around the boundary are also not comparable. For example, in VIKING20 a shift from fresher bottom salinities during a high NAO state to higher salinities during a low NAO state is clearly observed around Newfoundland and south along the eastern coast of the USA. In the EN4 dataset, however, this signal is not seen. Similarly, the strong change in the North Sea is only partially observed in EN4 and changes around Iceland are less pronounced than in VIKING20. Interestingly, the observed shift in VIKING20 from lower to higher

salinities in the Labrador Sea as the NAO weakens is also seen in the EN4 dataset; as is the opposite change in the centre of the basin. However, due to the lower data density in the central Labrador Sea, we attach lower confidence to this change.

In VIKING20 a strong anti-correlation between bottom potential temperature and salinity on the eastern and western continental shelves is observed. This is still seen in the EN4 bottom potential temperature dataset, albeit with the signal on the western shelf limited to the area around Newfoundland. However, in the EN4 salinity composite no discernible anti-correlation is observed between the eastern and western shelves.

8. Results: Spatial variability linked to SPG states

We now move on to discussing variability linked to changes in the strength of the SPG. A high SPG index represents a strong and expanded gyre, whilst a low index characterises a weaker and more contracted circulation. As the SPG index is an oceanic index, and changes in the real and modelled ocean may not be contemporaneous, it is not appropriate to use the observed SPG time series to interrogate the VIKING20 dataset. We considered extracting out a model-based SPG time series from VIKING20; however, the basin-averaged sea surface height field exhibits a drift after the mid-1990s which would redistribute the power among the principal components used to generate the SPG index. As such, we use only the observational SPG time series and examine changes in the EN4 dataset only.

For bottom potential temperature, a striking feature is the strong change around the northern and western boundaries of the subpolar North Atlantic (Figure 36). The Scottish slope region, the Greenland-Scotland Ridge, east and west of Greenland, the boundaries of the Labrador Sea, and moving southward to the area around Newfoundland and the eastern seaboard of the USA all exhibit warmer bottom temperatures during a weaker SPG and cooler conditions during a stronger SPG. A weaker but similar signal is observed in the northern North Sea whilst the southern North Sea appears to be anti-correlated. The interior of the Rockall Trough, Iceland Basin, Irminger Sea and Labrador Sea also seem to show warmer bottom temperatures during a weaker SPG although we note that data density here is lower. While there may be changes in the abyssal North Atlantic, Nordic Seas or Baffin Bay, the lack of data in these areas limit the identification of these signals in the observational record.

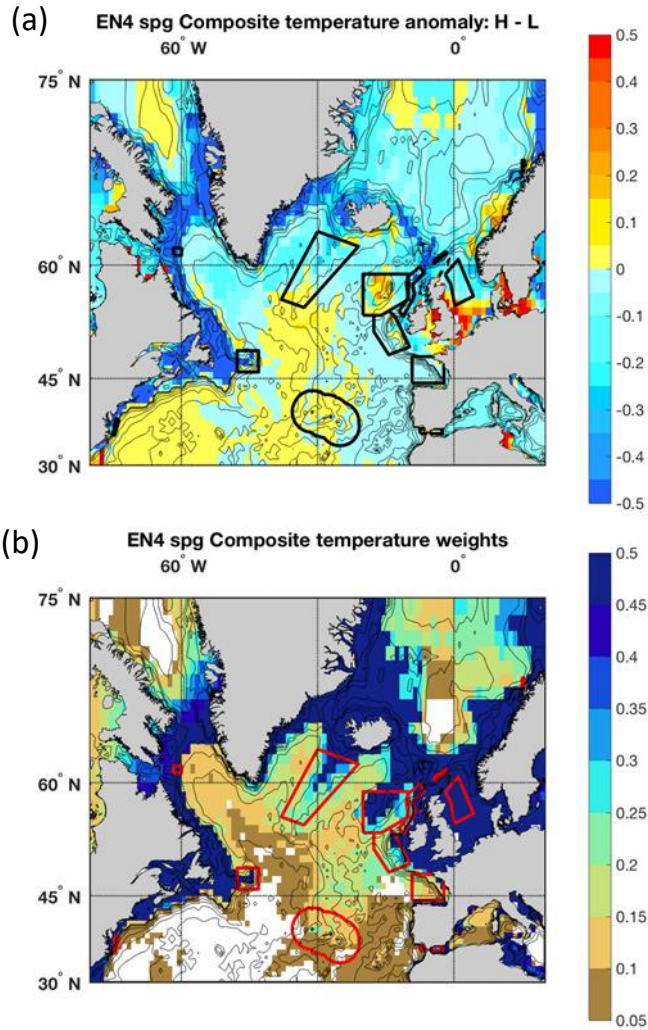


Figure 36. (a) SPG High minus Low map of bottom potential temperatures, T_{bot} ($^{\circ}$ C) in EN4 and (b) mean data weighting.

The EN4 data weighting ranges from 0 to 1 with 0 indicating no data availability.

Although bottom salinity also shows a change around the northern and western boundaries of the subpolar North Atlantic (Figure 37), this is less pronounced than for bottom potential temperature. Salinities again appear to be higher during a weaker SPG on the western European Shelf, Greenland-Scotland Ridge, east and west of Greenland and along the Canadian Shelf. The largest change, however, is around Newfoundland and further south on the eastern coast of the USA. Both the northern and southern North Sea shows an increase in salinities associated with a weakening SPG, with a similar salinification seen along the coast of Norway. Finally, whilst the interior of the Rockall Trough and Iceland Basin show an increase in bottom potential temperature with a reduction in the SPG, these areas show a decrease in bottom salinities for the same forcing. As the interior of the Irminger Sea and Labrador Sea show a bottom salinity change in phase with the bottom temperature

change, we are unsure whether the change in the Rockall Trough and Iceland Basin is a real signature of the NAO or due to aliasing.

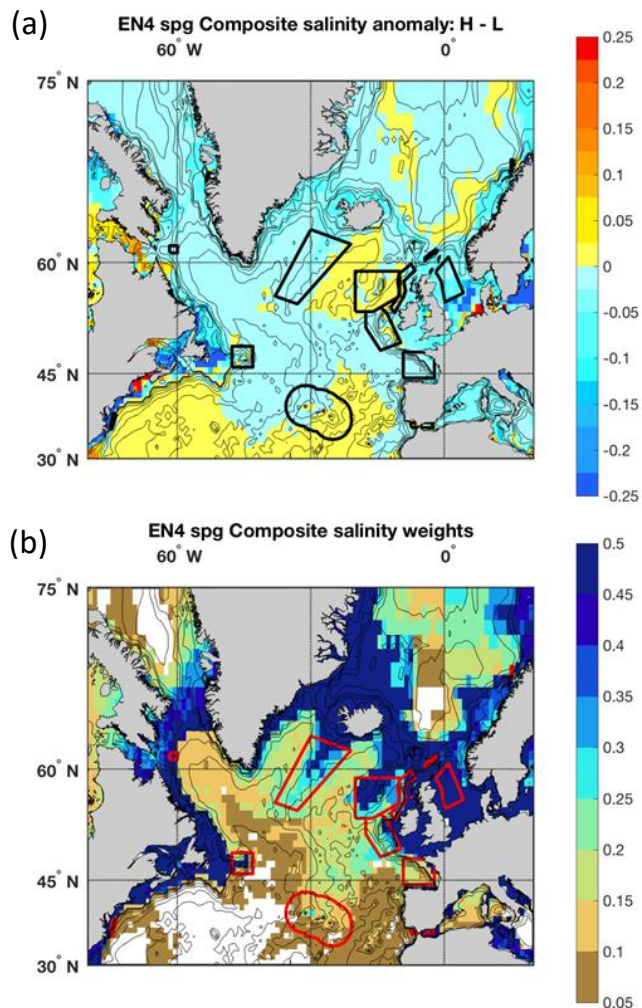


Figure 37. As figure 36 but for bottom salinity, *S_{bot}*.

9. Results: Spatial variability linked to AMO states

In this section, we present the spatial variability associated with a change in the AMO state. Again, as the AMO is an ocean-derived index, and changes in the real and modelled ocean may not be contemporaneous, it is not appropriate to use the observational index to interrogate the VIKING20 dataset. Although we considered the construction of an AMO index from VIKING20, we discounted it for two reasons. Firstly, the AMO index is calculated using sea surface temperatures over the entire North Atlantic (Enfield *et al.*, 2001); however, the VIKING20 nested model domain starts at 32 °N (Böning *et al.*, 2016). This makes the calculation of an AMO index from VIKING20 complex. Secondly, VIKING20 is an ocean-only model meaning that feedbacks between the ocean and atmosphere are

not fully represented. As work suggests that there is a requirement for fully-coupled models in order to represent important teleconnections (Ruprich-Robert *et al.*, 2017), we focus on the observational AMO index and present results from the EN4 dataset only (Figures 38-39).

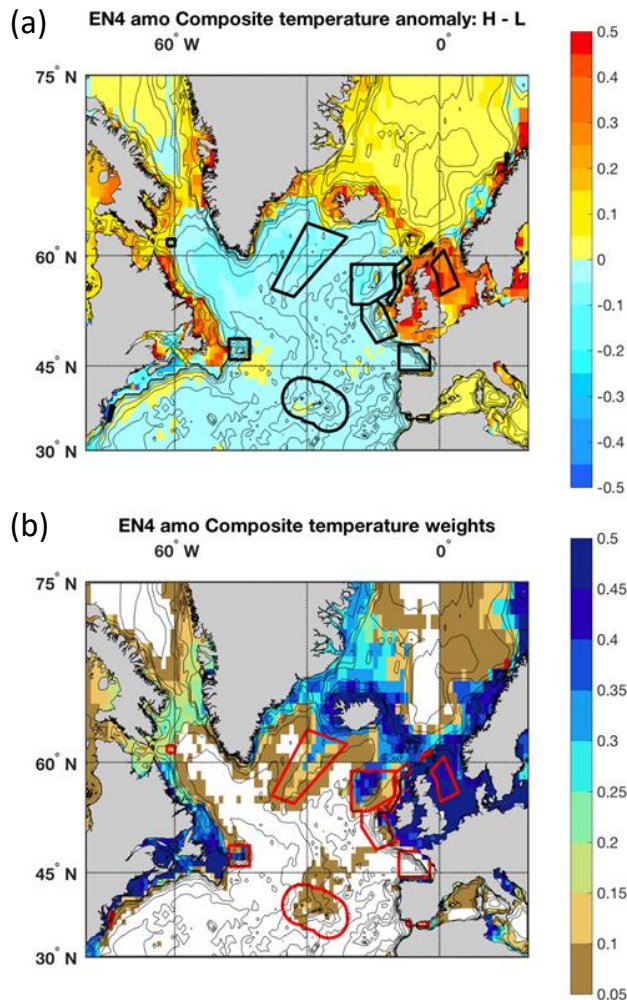


Figure 38. (a) AMO High minus Low map of bottom potential temperatures, T_{bot} (°C) in EN4 and (b) mean data weighting.

The EN4 data weighting ranges from 0 to 1 with 0 indicating no data availability.

The AMO index is defined by SST; as such we expect, in general, warmer SST during a high index and cooler SST during a low index. A somewhat similar picture of increased bottom potential temperatures is observed (Figure 38). Warmer conditions are observed over the Western European Shelf, Greenland-Scotland Ridge, east Greenland coast and the boundaries of the Labrador Sea during a high AMO. Warmer conditions are also observed around Newfoundland, although bottom potential temperatures further south along the eastern coast of the USA show an opposite signal with cooler conditions during a high AMO state. Although the majority of the Atlantic away from the

boundaries shows cooler temperatures during a high AMO, and warmer temperatures during a low AMO state, the lack of data in this region means this signal must be treated with caution.

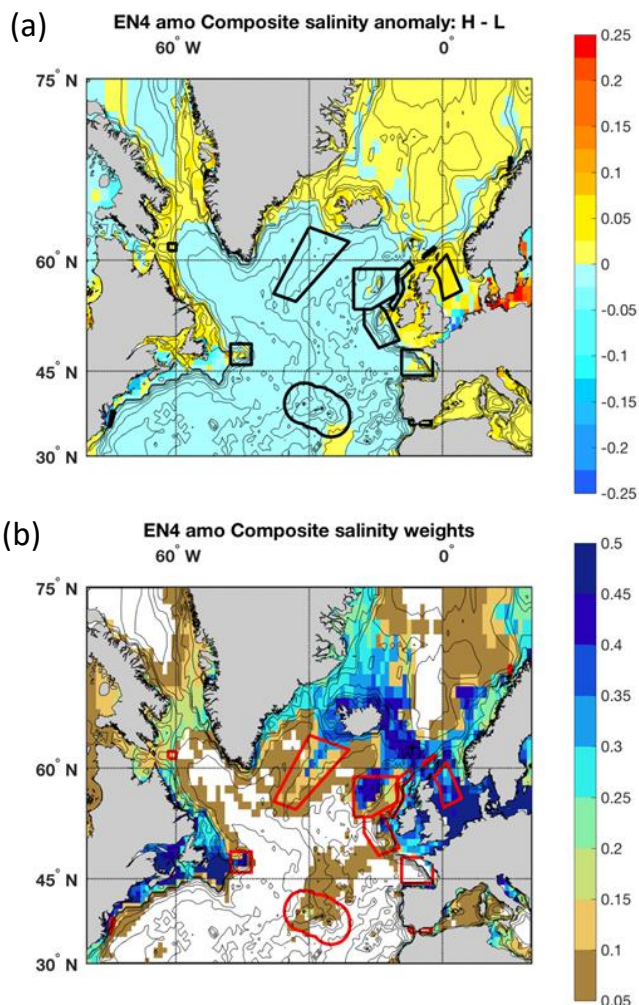


Figure 39. As figure 38 but for bottom salinity, *S_{bot}*.

An almost identical spatial pattern is observed in bottom salinity (Figure 39); however, the changes observed in the Baltic Sea are greater than those seen in the Atlantic muting the changes in the latter on Figure 39. During a high AMO, elevated bottom salinities are observed on the western European Shelf, the Greenland Scotland Ridge, along the east coast of Greenland and around the boundaries of the Labrador Sea. In a similar pattern to bottom potential temperatures, bottom salinities near Newfoundland are higher during a high AMO whilst salinities around Grand Banks and further south along the eastern coast of the USA are lower. One difference between bottom potential temperature and salinity is seen in the North Sea. Whilst the whole area shows warmer temperatures during a high AMO state, the northern and southern area shows an anti-correlation in terms of salinity. Finally, we raise the possibility that the signals seen for the AMO and SPG may not

be independent from one another due to the potential similarity between the two time series. This warrants further investigation.

10. Variability at case study sites

Having looked at changes associated with each climate index at basin-scale, we now examine changes at each case study in turn. For VIKING20, we examine changes associated with the NAO and the VIKING20 AMOC, whilst for EN4 we consider the NAO, the observed AMOC time-series along the OVIDE line, the SPG and the AMO. Mean conditions for the high and low periods of each climate index calculated using VIKING20 are shown in Appendix B, with those calculated using EN4 given in Appendix C. For all sites and variables, we note that the standard deviation about each mean is larger than the difference between the high and low states for a particular index.

We also caution the reader that most case study regions cover a range of depths (Table 1), which may be subject to different processes and signals, as well as lag periods. As such, changes at a particular depth may be different to the mean conditions for the entire case study site. Additionally, if signals at different depths are opposing, changes averaged across the case study as a whole may be muted, despite large changes in individual depth layers. Finally, as changes are often larger at shallower depths, case study averages are likely to be biased towards processes occurring higher in the water column. As such, we advise the reader to consider the results in this section in conjunction with Sections 6-9.

10.1 VIKING20

The High minus Low values calculated using VIKING20 are summarised in Figure 40. As it is not appropriate to use the AMO and SPG time-series to interrogate the VIKING20 dataset, we only explore changes related to the NAO and VIKING20 AMOC. It is important to note that the NAO composites are averaged over DJFM only, which may artificially elevate MLD changes in particular. A positive 'High minus Low' value indicates a deeper MLD / warmer / more saline conditions during the high climate state. Conversely, a negative 'High minus Low' value indicates a shallower MLD / cooler / fresher conditions during the high climate state.

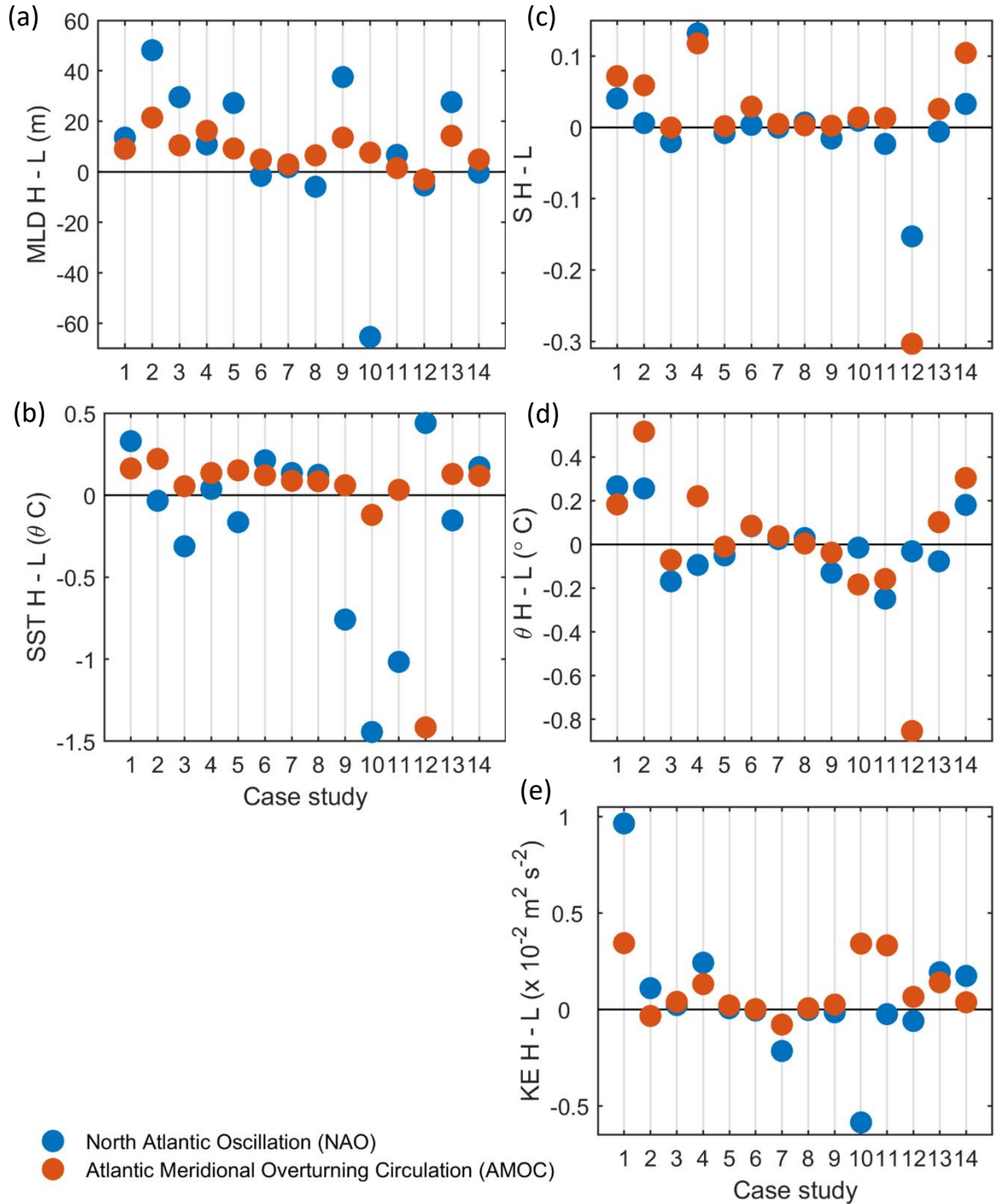


Figure 40. Summary of changes in VIKING20 associated with the NAO (blue) and AMOC (orange) at the 14 case study sites. Panels show High minus Low values for: (a) mixed layer depth MLD (m), (b) sea surface temperature SST ($^{\circ}\text{C}$), (c) bottom salinity S_{bot} , (d) bottom potential temperature T_{bot} ($^{\circ}\text{C}$), and (e) bottom kinetic energy KE_{bot} ($\times 10^{-2} \text{ m}^2 \text{ s}^{-2}$).

The largest changes in MLD are associated with the NAO at the majority of case studies, with the exception of case studies CS04, CS06, CS07 and CS014 where the AMOC is associated with the

biggest changes. CS04 and CS14 are both on the western European Shelf (Mingulay Reef and North Sea respectively), whilst CS06 and CS07 are also on the eastern boundary of the Atlantic (Bay of Biscay and Gulf of Cadiz / Alboran Sea respectively). The largest change in MLD is observed at CS10 (Davis Strait) for the NAO, where the mean MLD is 65 m deeper during a low NAO than a high NAO period. Changes exceeding 25 m are also seen at case studies CS02 (Western Scottish Slope), CS03 (Rockall Bank), CS05 (Porcupine Sea Bight), CS10 (Davis Strait) and CS13 (Scottish Slope). However, as changes have not been normalised by water depth, it is less likely that the largest changes will be seen at shallower case studies.

For SST, changes exceeding 1 °C are seen at CS10 (Davis Strait) and CS11 (Flemish Cap) for the NAO, and CS12 (USA Mid-Atlantic Canyons) for the AMOC. At CS10 and CS11, cooler conditions are seen during a high NAO, whilst at CS12 cooler SST values are observed during a high AMOC. A relatively large change (-0.76 °C) is also observed at CS09 (Reykjanes Ridge), again for the NAO. It is notable that CS10, CS11 and CS12 are all located in the western subpolar North Atlantic (Figure 1).

Moving now to examine bottom conditions, the largest changes in bottom salinity (> 0.1) are observed at the relatively shallow CS04 (Mingulay Reef), CS12 (USA Mid-Atlantic Canyons) and CS14 (North Sea). At CS04, the AMOC and NAO are associated with similar magnitude changes, whilst at CS12 and CS14 the AMOC is associated with the largest change. We also note that CS04 and CS12 are anti-correlated for both the NAO and AMOC: during a high NAO or AMOC, more saline bottom conditions are seen at CS04 on the eastern boundary, whilst fresher bottom conditions are seen at CS12 on the western boundary.

The largest change in bottom potential temperature (-0.85 °C) is observed at CS12 (USA Mid-Atlantic Canyons) for the AMOC, indicating cooler bottom conditions during a high AMOC. A large change is also seen at CS02 (Western Scottish Slope) where bottom conditions are 0.52 °C warmer during a high AMOC relative to a low AMOC. Interestingly, the strong anti-correlation observed for bottom salinity and the NAO between CS04 (Mingulay Reef) and CS12 (USA Mid-Atlantic Canyons), does not exist for bottom temperatures. However, CS04 and CS12 still show an opposite response with the AMOC: during a high AMOC, bottom temperatures are warmer at CS04 and cooler at CS12.

The largest changes in bottom kinetic energy ($> 0.5 \times 10 \text{ m}^2\text{s}^{-2}$) are observed at CS01 (LoVe Observatory) and CS10 (Davis Strait) and are associated with the NAO. Both these case study sites are located in energetic boundary currents on the Norwegian Slope and Labrador Sea boundary

respectively. Interestingly, CS01 shows more energetic conditions during a high NAO, whilst CS10 shows lower kinetic energy values.

10.2 EN4

We now discuss the changes seen in bottom conditions within EN4 (Figure 41). For this dataset we compare each of the four climate indices, but only look at bottom salinity and potential temperature. Again, a positive 'High minus Low' value indicates warmer / more saline bottom conditions during the high climate state, with a negative value indicating cooler / fresher conditions.

Changes in the observational EN4 dataset are smaller than those observed in VIKING20 model output, although we also note that only the NAO values are directly comparable. For both bottom salinity and bottom potential temperature, the largest changes are seen at the shallow CS04 (Mingulay Reef) and CS14 (North Sea) sites. Here, large positive changes are associated with both the AMO and SPG. Relatively large changes are also seen at CS07 (Gulf of Cadiz / Alboran Sea) for both the AMOC and NAO, although these are opposite in sign.

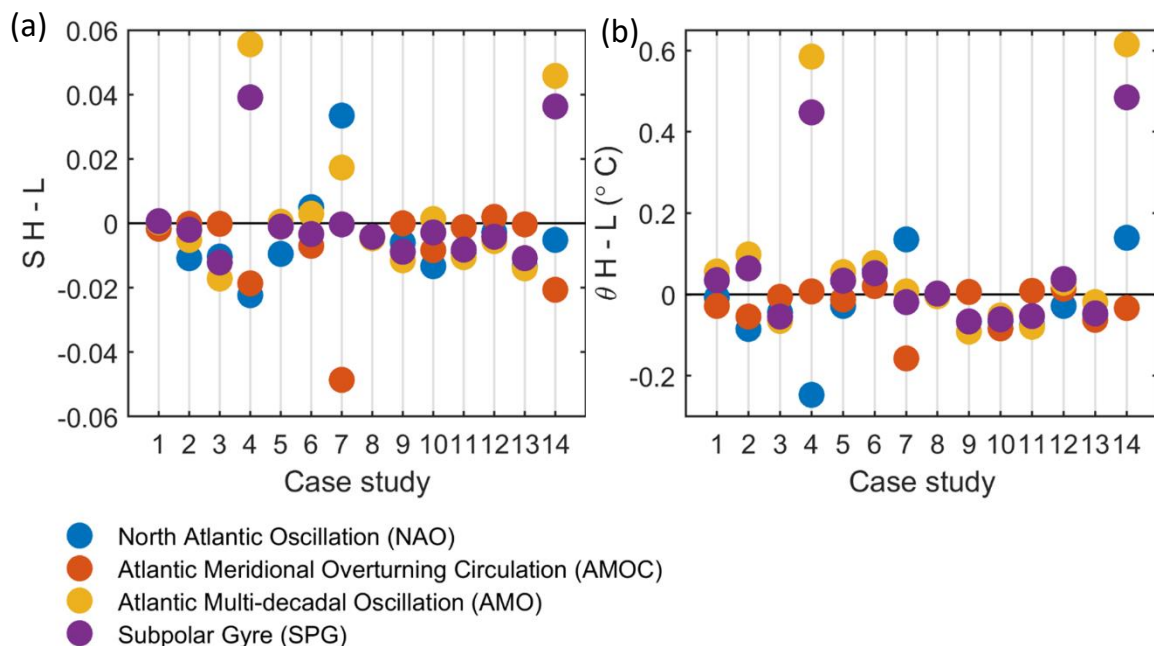


Figure 41. Summary of changes in EN4 associated with the NAO (blue), AMOC (orange), AMO (yellow) and SPG (purple) at the 14 case study sites. Panels show High minus Low values for: (a) bottom salinity S_{bot} , and (b) bottom potential temperature T_{bot} (°C). Case studies were the weighting is <0.05 for either the high or low periods are not shown. Please note the different y-axes compared to figure 40.

We now discuss changes at each case study in turn. **CS01** is situated on the Norwegian Coast. Here, changes in bottom salinity for all climate indices are small, whilst the AMO is associated with the largest change in bottom potential temperature: during a high AMO, bottom conditions are 0.06 °C warmer.

At **CS02**, on the western Scottish Slope, the largest change in bottom salinity is associated with the NAO (-0.011), this change is twice as large as that associated with the AMO (-0.005). All climate indices are associated with relatively large changes in θ_{bot} although the AMO is associated with the largest change (0.10 °C). The NAO and AMOC have cooler θ_{bot} values during the high states, whilst the high states of the AMO and SPG are associated with warmer θ_{bot} values.

CS03 is at Rockall Bank. Here, the largest changes in both bottom salinity (-0.017) and bottom potential temperature (-0.07 °C) are associated with the AMO.

CS04, which has an average depth of 196 m and covers the Mingulay Reef complex to the west of Scotland, shows large changes. The NAO and AMOC have fresher bottom values during a high state, whilst the AMO and SPG have more saline conditions. A similar pattern is seen for bottom potential temperature for the NAO, AMO and SPG, but changes associated with the AMOC are small. During a high NAO, cooler bottom conditions are seen, whilst during a high AMO and SPG, warmer bottom temperature are observed. However, the largest change in both θ_{bot} and S_{bot} is associated with the AMO (0.58 °C and 0.056 respectively).

At **CS05**, on the Porcupine Sea Bight, changes in bottom conditions between high and low states of all climate indices are relatively small. The NAO is associated with the largest change in bottom salinity (-0.009); however, the largest change in bottom potential temperature (0.06 °C) is associated with the AMO.

CS06 is in the Bay of Biscay. Here, changes in both bottom salinity and bottom potential temperature are again relatively small, with the largest change (-0.007, 0.08 °C) being associated with the AMOC and AMO respectively.

CS07 is located in the Gulf of Cadiz / Alboran Sea and has a mean depth of 697 m. The largest change in bottom salinity (-0.049) at this site is associated with the AMOC, although the NAO and AMO are also associated with relatively large changes (0.034 and 0.017 respectively). In contrast, the SPG is

associated with a change smaller than instrumental accuracy. Changes in bottom potential temperature are less pronounced, with only the NAO and AMOC being associated with changes exceeding 0.1 °C (0.14 °C and -0.16 °C respectively).

CS08 is situated around the Azores and is the deepest site with a mean depth of 3064 m. There is insufficient data to assess changes associated with the NAO and AMOC, as mean weightings for the high and low periods of these indices are less than the cut-off value of 0.05. As expected for such a deep site, changes associated with the AMO and SPG are very small (less than ± 0.005 and ± 0.01 °C).

At **CS09**, which is situated on the Reykjanes Ridge, changes in bottom salinity are only seen for the NAO, AMO and SPG. For bottom potential temperature, changes exceeding the instrumental accuracy are observed for all climate indices, although the change associated with the AMOC is an order of magnitude smaller than those associated with the NAO, AMO and SPG. The largest change in both bottom salinity and bottom potential temperature is associated with the AMO (-0.012 and -0.09 °C respectively). During a high AMOC, cooler and less saline bottom conditions are observed.

CS10 is situated in the Davis Strait. All climate indices show changes exceeding instrumental accuracy for bottom salinity, with the largest change (-0.008) being associated with the NAO. Although the largest change in bottom potential temperature (-0.084) is seen for the AMOC, all four indices produce similar magnitude changes.

CS11, which is situated on the Flemish Cap, shows negative H minus L bottom salinity values for all the climate indices. However, the change associated with the AMOC (-0.001) is smaller than that associated with the other three indices (NAO -0.009, AMO -0.010, SPG -0.008). The NAO, AMO and SPG also produce similar magnitude changes in bottom potential temperature (-0.07 °C, -0.08 °C and -0.05 °C respectively).

At **CS12**, which covers the USA mid-Atlantic Canyons, the largest changes in bottom salinity are associated with the AMO (-0.006) and SPG (-0.004). For both of these indices, fresher bottom conditions are seen during a high state. The largest change in bottom potential temperature is associated with the SPG (0.04 °C) although this is opposite in sign for bottom salinity: i.e. during a high AMO, CS12 has fresher but warmer bottom conditions.

At **CS13**, on the European Slope, the NAO, AMO and SPG are all associated with similar magnitude changes in bottom salinity (-0.01), whilst the change associated with the AMOC is smaller than instrumental accuracy. In contrast, the largest change in bottom potential temperature (-0.06 °C) is associated with the AMOC, although the changes associated with the NAO and SPG are only slightly smaller (-0.05 °C for both).

CS14 is in the North Sea and is the shallowest site with a mean depth of 99 m. The largest changes in bottom salinity are associated with the AMO and SPG with changes of 0.046 and 0.36 respectively. In contrast, the AMOC is associated with a negative High minus Low value (-0.021) and the AMOC only shows a small change (-0.005). The AMO and SPG are also associated with large positive changes in bottom potential temperature (0.61 °C and 0.49 °C respectively), whilst the NAO shows a smaller positive change (0.14 °C) and the AMOC a small negative change (-0.03 °C).

11. Discussion and summary

The long-term mean conditions presented in section 3 provide a baseline in which to investigate variability associated with the AMO, AMOC, NAO and SPG in the North Atlantic region. Observational data obtained from the EN4 dataset compare very well to output from the VIKING20 model.

Interestingly, VIKING20 shows a maximum in bottom potential temperature, salinity and kinetic energy between approximately 200 and 2000 m depth along the eastern boundary of the North Atlantic (Figures 8-9). We suggest that this feature, which is too small to be resolved by the 1° x 1° EN4 dataset, may be linked to vertical heave of water and large-scale internal waves. As VIKING20 does not include internal tides, additional forcing from the interaction of these with the sloping bathymetry may amplify the signal. As expected, the seasonal signal is largest for surface properties such as SST and mixed layer depth (Figures 13-14). Whilst a seasonal signal is observed for bottom potential temperature and salinity at shallower sites, at deeper sites the cycle is very small or not discernible (Figures 15-18). Additionally, the seasonal cycles in bottom potential temperature and salinity are larger in VIKING20 than the observational dataset.

Having established these baseline characteristics, we moved on to investigating the effect of four climate indices pertinent to the North Atlantic: the AMOC, NAO, SPG and AMO. Although we consider each of these indices in isolation using the composite method of Duchez *et al.* (2016), we note that the indices are unlikely to be fully independent of one another. For example the SPG index has, at times, been shown to correlate with the NAO index (Lozier and Stewart, 2008), whilst

variations in the AMOC has been linked to changes in Atlantic sea surface temperatures (Buckley and Marshall, 2016). Additionally, we note a possible similarity between the AMO and SPG index, albeit with a much shorter SPG record.

For the AMOC, the EN4 and VIKING20 datasets generally compare well around the more observation-rich ocean boundaries, but less well for the abyssal areas where little or no observations exist (Figures 21-28). It should be noted that there were slight differences in the smoothing periods used, as well as the definition of the AMOC, which may have influenced the comparison.

Concentrating on bottom conditions, VIKING20 shows a clear anti-correlation between the western European Shelf and eastern USA coastal areas for both potential temperature and salinity. During a high AMOC period, the bottom conditions on the western European Shelf are warmer and saltier, whilst the conditions on the eastern coast of the USA are cooler and fresher (Figures 21-22). This signal is less clearly observed in the EN4 dataset. Additionally, warmer and saltier water is seen in the western basin of the deep Atlantic south of about 55 °N during a high AMOC, whilst cooler and fresher water is observed in the eastern portion. It is not possible to observe this change in the observational dataset due to extremely limited data coverage.

The NAO VIKING20 composites (Figures 29-35) have some similarities to the AMOC composites; namely the split between warmer and saltier bottom conditions in the western deep Atlantic south of ~ 55 °N during high NAO periods compared to cooler and fresher conditions in the eastern basin. However, the NAO composites also show changes in the Irminger Sea that are not observed in the AMOC maps. During a high NAO bottom potential temperatures in the Irminger Sea are cooler and fresher, swapping to warmer and saltier during low NAO periods. Interestingly, SST shows more of a north-south split with, in general, lower values in the subpolar North Atlantic during a high NAO and higher values south of approximately 45 °N, and vice versa for a low NAO. As for the AMOC, bottom potential temperature and salinity show an anti-correlation between the western European Shelf and area around Grand Banks. Again, warmer and saltier conditions are observed on the western European Shelf in the high NAO composite and around Grand Banks during the low NAO. This east-west anti-correlation is also seen in the SST NAO composites. Both the AMOC and NAO show changes in bottom kinetic energy, in the main concentrated towards the boundaries of the ocean. However, for the NAO the changes are anti-correlated between the Labrador Sea and Irminger Sea; and also between the North Sea and coast of Norway, and along the Faroes-Iceland Ridge.

For the AMO and SPG we focus on the signal within the observational dataset only. The highest confidence is attached to changes seen in the more data-rich areas, namely the eastern and western boundaries and Greenland-Scotland Ridge region. We do not discuss changes in the data-sparse abyssal regions. The most striking feature in the SPG high-minus-low maps are the changes stretching from the Scottish Slope region, along the Greenland-Scotland Ridge and cyclonically around the Labrador Sea and into the Grand Banks area (Figures 36-37). During a high SPG (i.e. strong and expanded gyre), bottom potential temperatures are cooler and fresher with the opposite signal during a low SPG index. The AMO shows a similar spatial pattern with warmer and more saline conditions during the high AMO composite (Figures 38-39). This is perhaps unsurprising if the two indices do indeed share similarities (i.e. a positive SPG index is associated with a negative AMO index and vice versa). However, we note that the observational dataset can only be used round the data-rich boundaries and that any differences (or similarities) in the deeper areas have therefore not been investigated.

Finally, we compared the effect of different climate indices across case study sites. Broadly speaking the NAO was associated with the largest changes in mixed layer depth in the subpolar region (Figure 40), although this may be an artefact caused by the NAO composites being created by averaging DJFM months only. The largest changes in SST in VIKING20 were observed at the CS10, CS11 and CS12 which are all in the western subpolar gyre (Figure 40). Changes in bottom salinity and bottom potential temperature were larger in VIKING20 than the observational EN4 dataset. In EN4, the largest changes in bottom salinity were at the shallow case studies located on the eastern boundary: CS04, CS07 and CS14 (Figure 41). Interestingly, a similar signal at the shallow sites on the western boundary (e.g. CS10 and CS12) was absent. The largest changes in bottom potential temperature in EN4 were again at CS04 and CS14.

This report examines the signature of four pertinent climate indices to oceanic conditions across the North Atlantic region, and is the first to show that climate indices are associated with spatially-coherent signals in bottom conditions as well as upper ocean properties. Although changes in bottom conditions are relatively small, due to the multi-annual nature of the climate indices any changes may persist for several years. As such, vulnerable marine ecosystems may be exposed to sustained changes in mean conditions, with this deviation in the baseline also altering the likelihood of extreme events such as marine heat waves. Any changes have the potential to effect sessile deep-sea ecosystems to a greater extent than mobile pelagic species. Thus, a thorough knowledge of

natural variability is essential for the understanding of deep-sea ecosystems, predicting their response to future changes, and evaluation of management frameworks.

Acknowledgements

We thank Dr E Frajka-Williams (NOC) for kindly providing her extension to the RAPID overturning time series. We also acknowledge the help of Dr M Toberman (SAMS) for his help with the initial extraction and formation of data from the EN4 database.

Appendix A: Seasonal signal of climate indices

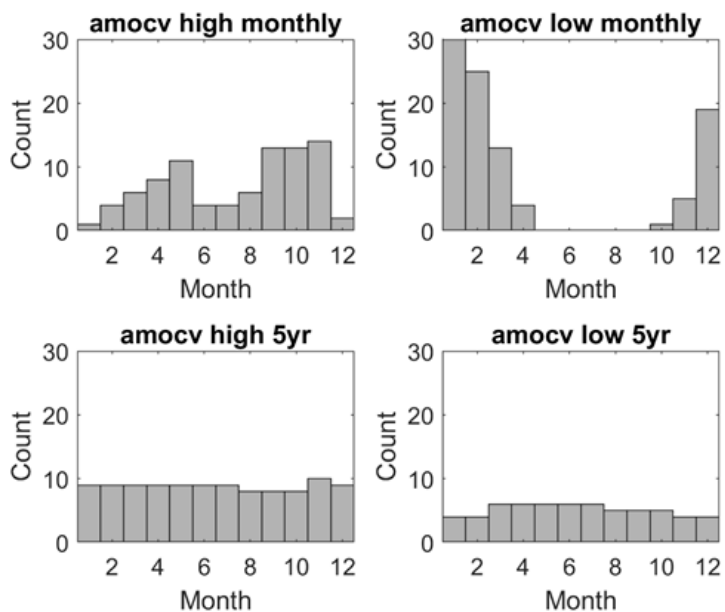


Figure A1. Seasonal signal associated with high and low periods in the VIKING20 AMOC time series.

(top): monthly averaged time series, (bottom): five-year smoothed time series.

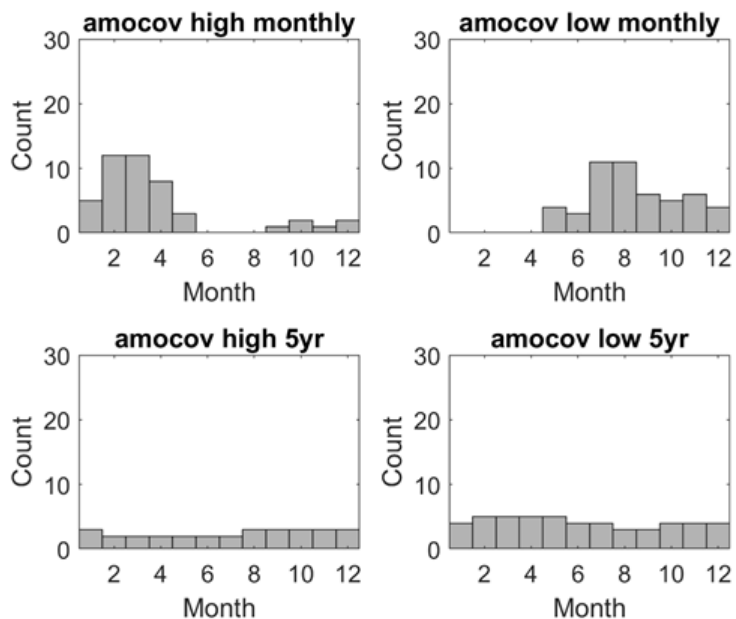


Figure A2. As figure A1 but for AMOC along the OVIDE section.

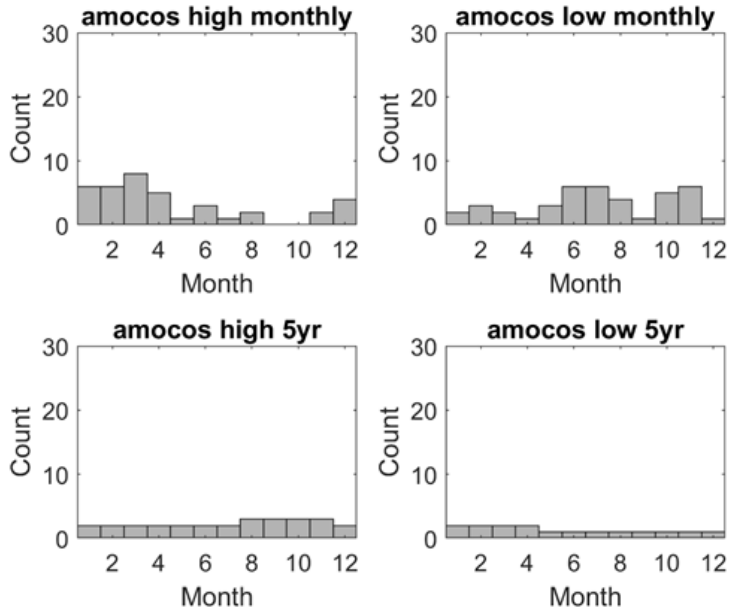


Figure A3. Figure A2. As figure A1 but for AMOC along the OSNAP section.

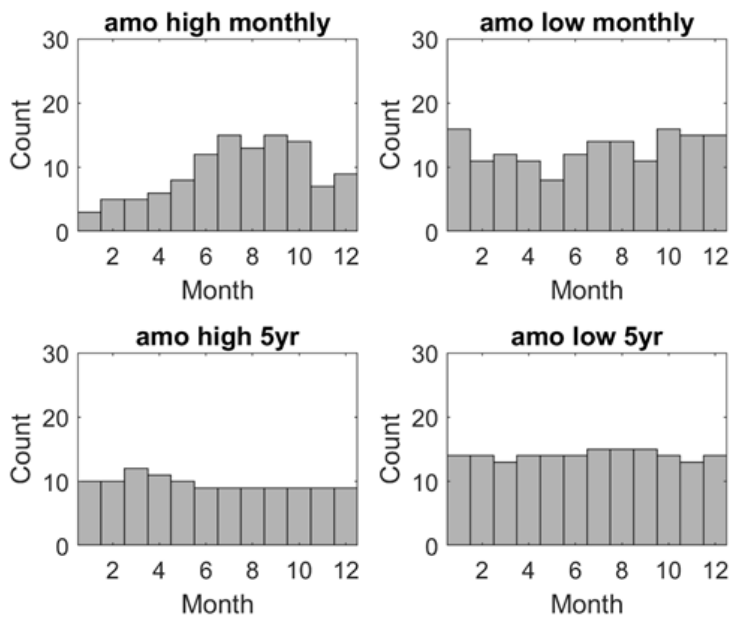


Figure A4. Figure A2. As figure A1 but for the AMO index.

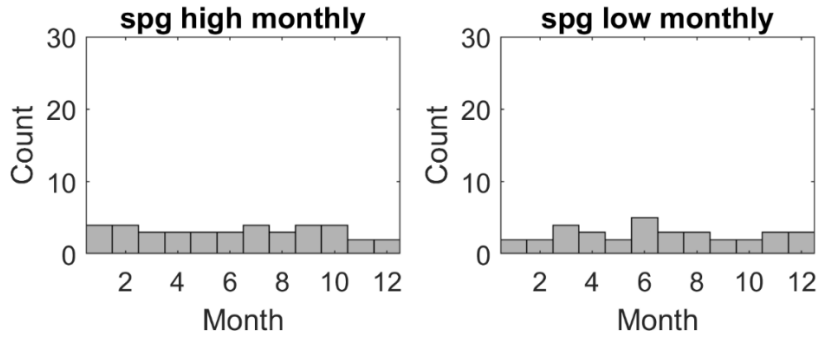


Figure A5. Seasonal signal associated with high and low periods in the monthly-averaged SPG time series.

Appendix B: Variability associated with climate indices in VIKING20

Case Study 1 (LoVe Observatory)

	MLD (m)	SST (°C)	T _{bot} (°C)	S _{bot}	KE _{bot} (10 ⁻² m ² s ²)
AMOC (VIKING20)					
high	60 ± 41	5.5 ± 2.2	3.1 ± 0.7	27.88 ± 0.08	1.5 ± 1.0
low	51 ± 34	5.3 ± 2.3	3.0 ± 0.7	27.81 ± 0.09	1.1 ± 0.7
NAO					
high	97 ± 26	4.9 ± 1.1	2.9 ± 0.4	27.90 ± 0.04	2.6 ± 1.2
low	82 ± 31	4.6 ± 1.2	2.6 ± 0.5	27.86 ± 0.07	1.7 ± 0.7

Table B1. Mean ± standard deviation for high and low years associated with the 5year smoothed time-series of each climate index at case study site 1 in VIKING20.

Climate indices investigated are: the strength of the Atlantic Meridional Overturning Circulation (AMOC) in VIKING20, and the North Atlantic Oscillation (NAO).

Key physical variables investigated are: mixed layer depth (MLD), sea surface temperature (SST), bottom potential temperature (T_{bot}), bottom salinity (S_{bot}), and bottom kinetic energy (KE_{bot}).

Case Study 2 (Western Scottish Slope)

	MLD (m)	SST (°C)	T_{bot} (°C)	S_{bot}	KE_{bot} (10⁻² m²s⁻²)
AMOC (VIKING20)					
high	139 ± 108	9.4 ± 1.2	3.8 ± 0.6	35.15 ± 0.03	1.1 ± 0.3
low	117 ± 95	9.2 ± 1.3	3.3 ± 0.6	35.09 ± 0.03	1.1 ± 0.3
NAO					
high	290 ± 65	8.4 ± 0.5	4.2 ± 0.6	35.16 ± 0.03	1.3 ± 0.4
low	237 ± 58	8.5 ± 0.5	4.0 ± 0.5	35.15 ± 0.04	1.2 ± 0.3

Table B2. As for Table B1 but for case study 2.

Case Study 3 (Rockall Bank)

	MLD (m)	SST (°C)	T_{bot} (°C)	S_{bot}	KE_{bot} (10⁻² m²s⁻²)
AMOC (VIKING20)					
high	180 ± 160	10.2 ± 1.2	5.6 ± 0.1	35.17 ± 0.01	0.1 ± 0.0
low	169 ± 161	10.2 ± 1.3	5.7 ± 0.1	35.17 ± 0.01	0.1 ± 0.0
NAO					
high	371 ± 121	9.0 ± 0.4	5.6 ± 0.1	35.17 ± 0.01	0.1 ± 0.0
low	334 ± 112	9.4 ± 0.4	5.8 ± 0.1	35.20 ± 0.02	0.1 ± 0.0

Table B3. As for Table B1 but for case study 3.

Case Study 4 (Mingulay Reef)

	MLD (m)	SST (°C)	T_{bot} (°C)	S_{bot}	KE_{bot} (10⁻² m²s⁻²)
AMOC (VIKING20)					
high	74 ± 40	10.0 ± 2.1	9.1 ± 1.5	35.13 ± 0.14	0.5 ± 0.5
low	57 ± 40	9.8 ± 2.3	8.8 ± 1.4	35.02 ± 0.13	0.4 ± 0.5
NAO					
high	113 ± 18	8.2 ± 1.0	8.1 ± 1.0	35.17 ± 0.14	0.9 ± 0.5
low	102 ± 27	8.3 ± 1.1	8.2 ± 1.1	35.04 ± 0.19	0.7 ± 0.6

Table B4. As for Table B1 but for case study 4.

Case Study 5 (Porcupine Sea Bight)

	MLD (m)	SST (°C)	T_{bot} (°C)	S_{bot}	KE_{bot} (10⁻² m²s⁻²)
AMOC (VIKING20)					
high	125 ± 112	12.0 ± 1.6	5.6 ± 0.1	35.20 ± 0.01	0.1 ± 0.0
low	116 ± 109	11.8 ± 1.7	5.6 ± 0.0	35.20 ± 0.01	0.1 ± 0.0
NAO					
high	261 ± 96	10.6 ± 0.6	5.7 ± 0.1	35.20 ± 0.01	0.1 ± 0.0
low	229 ± 83	10.8 ± 0.7	5.7 ± 0.1	35.21 ± 0.01	0.1 ± 0.0

Table B5. As for Table B1 but for case study 5.

Case Study 6 (Bay of Biscay)

	MLD (m)	SST (°C)	T_{bot} (°C)	S_{bot}	KE_{bot} (10⁻² m²s⁻²)
AMOC (VIKING20)					
high	55 ± 39	13.6 ± 2.2	5.5 ± 0.2	33.25 ± 0.03	0.1 ± 0.0
low	51 ± 39	13.5 ± 2.3	5.4 ± 0.2	33.22 ± 0.03	0.0 ± 0.0
NAO					
high	101 ± 17	12.0 ± 0.8	5.5 ± 0.2	33.22 ± 0.03	0.1 ± 0.0
low	102 ± 19	11.8 ± 0.9	5.4 ± 0.2	33.22 ± 0.03	0.1 ± 0.0

Table B6. As for Table B1 but for case study 6.

Case Study 7 (Gulf of Cadiz / Alboran Sea)

	MLD (m)	SST (°C)	T_{bot} (°C)	S_{bot}	KE_{bot} (10⁻² m²s⁻²)
AMOC (VIKING20)					
high	32 ± 20	15.6 ± 2.0	11.6 ± 0.1	32.09 ± 0.03	2.6 ± 0.3
low	29 ± 19	15.6 ± 2.1	11.5 ± 0.1	32.08 ± 0.02	2.7 ± 0.3
NAO					
high	57 ± 9	13.9 ± 0.7	11.5 ± 0.1	32.10 ± 0.01	2.6 ± 0.3
low	55 ± 7	13.8 ± 0.8	11.5 ± 0.1	32.10 ± 0.03	2.9 ± 0.4

Table B7. As for Table B1 but for case study 7.

Case Study 8 (Azores)

	MLD (m)	SST (°C)	T_{bot} (°C)	S_{bot}	KE_{bot} (10⁻² m²s⁻²)
AMOC (VIKING20)					
high	57 ± 43	18.4 ± 2.4	3.2 ± 0.0	34.92 ± 0.01	0.0 ± 0.0
low	51 ± 43	18.3 ± 2.7	3.2 ± 0.0	34.92 ± 0.00	0.0 ± 0.0
NAO					
high	107 ± 18	16.5 ± 0.9	3.2 ± 0.0	34.93 ± 0.00	0.0 ± 0.0
low	112 ± 22	16.4 ± 1.1	3.1 ± 0.0	34.92 ± 0.01	0.0 ± 0.0

Table B8. As for Table B1 but for case study 8.

Case Study 9 (Reykjanes Ridge)

	MLD (m)	SST (°C)	T_{bot} (°C)	S_{bot}	KE_{bot} (10⁻² m²s⁻²)
AMOC (VIKING20)					
high	201 ± 162	7.8 ± 1.3	4.0 ± 0.1	35.09 ± 0.01	0.4 ± 0.1
low	188 ± 166	7.7 ± 1.3	4.1 ± 0.0	35.09 ± 0.00	0.4 ± 0.0
NAO					
high	389 ± 111	6.5 ± 0.5	4.0 ± 0.1	35.08 ± 0.01	0.4 ± 0.1
low	345 ± 81	7.4 ± 0.5	4.1 ± 0.1	35.10 ± 0.01	0.4 ± 0.1

Table B9. As for Table B1 but for case study 9.

Case Study 10 (Davis Strait)

	MLD (m)	SST (°C)	T_{bot} (°C)	S_{bot}	KE_{bot} (10⁻² m²s⁻²)
AMOC (VIKING20)					
high	63 ± 76	1.1 ± 2.3	2.7 ± 0.3	34.89 ± 0.02	2.1 ± 0.6
low	56 ± 59	1.3 ± 2.4	2.9 ± 0.2	34.88 ± 0.02	1.8 ± 0.4
NAO					
high	59 ± 53	-0.7 ± 1.3	2.9 ± 0.2	34.91 ± 0.01	1.7 ± 0.6
low	128 ± 87	0.8 ± 1.5	2.9 ± 0.2	34.90 ± 0.02	2.3 ± 0.6

Table B10. As for Table B1 but for case study 10.

Case Study 11 (Flemish Cap)

	MLD (m)	SST (°C)	T_{bot} (°C)	S_{bot}	KE_{bot} (10⁻² m²s⁻²)
AMOC (VIKING20)					
high	41 ± 41	5.5 ± 2.5	3.3 ± 0.1	34.95 ± 0.01	1.7 ± 0.3
low	39 ± 34	5.3 ± 2.4	3.4 ± 0.1	34.93 ± 0.01	1.3 ± 0.2
NAO					
high	82 ± 26	4.9 ± 1.3	3.3 ± 0.1	34.93 ± 0.01	1.6 ± 0.4
low	74 ± 31	4.6 ± 1.3	3.5 ± 0.2	34.96 ± 0.02	1.6 ± 0.4

Table B11. As for Table B1 but for case study 11.

Case Study 12 (USA Mid-Atlantic Canyons)

	MLD (m)	SST (°C)	T_{bot} (°C)	S_{bot}	KE_{bot} (10⁻² m²s⁻²)
AMOC (VIKING20)					
high	16 ± 10	14.0 ± 5.3	5.8 ± 0.9	34.21 ± 0.15	0.5 ± 0.3
low	19 ± 16	15.4 ± 5.3	6.7 ± 0.9	34.51 ± 0.17	0.5 ± 0.3
NAO					
high	27 ± 9	9.8 ± 2.2	5.6 ± 0.8	34.14 ± 0.14	0.7 ± 0.4
low	32 ± 11	9.4 ± 2.4	5.7 ± 0.8	34.30 ± 0.22	0.7 ± 0.4

Table B12. As for Table B1 but for case study 12.

Case Study 13 (Scottish Slope)

	MLD (m)	SST (°C)	T_{bot} (°C)	S_{bot}	KE_{bot} (10⁻² m²s⁻²)
AMOC (VIKING20)					
high	176 ± 155	10.6 ± 1.3	6.8 ± 0.2	35.25 ± 0.01	0.5 ± 0.3
low	162 ± 151	10.4 ± 1.4	6.7 ± 0.2	35.22 ± 0.01	0.3 ± 0.2
NAO					
high	347 ± 113	9.5 ± 0.5	6.7 ± 0.2	35.24 ± 0.01	0.8 ± 0.3
low	312 ± 108	9.7 ± 0.5	6.8 ± 0.2	35.25 ± 0.03	0.6 ± 0.2

Table B13. As for Table B1 but for case study 13.

Case Study 14 (North Sea)

	MLD (m)	SST (°C)	T_{bot} (°C)	S_{bot}	KE_{bot} (10⁻² m²s⁻²)
AMOC (VIKING20)					
high	59 ± 35	8.9 ± 2.2	7.8 ± 1.4	35.21 ± 0.05	0.3 ± 0.2
low	54 ± 36	8.8 ± 2.3	7.5 ± 1.4	35.11 ± 0.03	0.3 ± 0.1
NAO					
high	94 ± 2	7.3 ± 1.1	7.3 ± 1.1	35.22 ± 0.07	0.6 ± 0.2
low	94 ± 2	7.2 ± 1.2	7.2 ± 1.2	35.19 ± 0.08	0.4 ± 0.1

Table B14. As for Table B1 but for case study 14.

Appendix C: Variability associated with climate indices in EN4

Case Study 1 (LoVe Observatory)

	T_{bot} (°C)	S_{bot}
AMO		
high	-1.0 ± 0.0	34.91 ± 0.01
low	-1.0 ± 0.0	34.91 ± 0.01
AMOC (OVIDE)		
high	-1.0 ± 0.0	34.91 ± 0.01
low	-1.0 ± 0.0	34.91 ± 0.01
NAO		
high	-1.0 ± 0.0	34.91 ± 0.01
low	-1.0 ± 0.0	34.91 ± 0.01
SPG		
high	-1.0 ± 0.0	34.91 ± 0.01
low	-1.0 ± 0.0	34.91 ± 0.01

Table C1. Mean \pm standard deviation for high and low years associated with the 5year smoothed time-series of each climate index at case study site 1 in EN4.

Climate indices investigated are: the Atlantic Multi-decadal Oscillation (AMO); strength of the Atlantic Meridional Overturning Circulation (AMOC) along the OVIDE section, the North Atlantic Oscillation (NAO); and strength of the Subpolar Gyre (SPG).

Key physical variables investigated are: bottom potential temperature (T_{bot}), and bottom salinity (S_{bot}).

Case Study 2 (Western Scottish Slope)

	T_{bot} (°C)	S_{bot}
AMO		
high	-0.7 ± 0.1	34.91 ± 0.01
low	-0.8 ± 0.9	34.92 ± 0.02
AMOC (OVIDE)		
high	-0.8 ± 0.1	34.91 ± 0.01
low	-0.8 ± 0.1	34.91 ± 0.02
NAO		
high	-0.9 ± 0.0	34.90 ± 0.01
low	-0.8 ± 0.1	34.91 ± 0.01
SPG		
high	-0.7 ± 0.1	34.91 ± 0.01
low	-0.8 ± 0.1	34.91 ± 0.01

Table C2. As for Table C1 but for case study 2.

Case Study 3 (Rockall Bank)

	T_{bot} (°C)	S_{bot}
AMO		
high	3.6 ± 0.1	34.96 ± 0.01
low	3.7 ± 0.1	34.98 ± 0.01
AMOC (OVIDE)		
high	3.4 ± 0.0	34.96 ± 0.01
low	3.6 ± 0.0	34.96 ± 0.02
NAO		
high	3.6 ± 0.1	34.96 ± 0.01
low	3.6 ± 0.1	34.97 ± 0.02
SPG		
high	3.6 ± 0.1	34.96 ± 0.01
low	3.6 ± 0.1	34.97 ± 0.01

Table C3. As for Table C1 but for case study 3.

Case Study 4 (Mingulay Reef)

	T_{bot} (°C)	S_{bot}
AMO		
high	9.9 ± 0.4	35.41 ± 0.02
low	9.3 ± 0.4	35.35 ± 0.03
AMOC (OVIDE)		
high	9.8 ± 0.3	35.38 ± 0.01
low	9.8 ± 0.5	35.40 ± 0.04
NAO		
high	9.3 ± 0.3	35.36 ± 0.02
low	9.6 ± 0.5	35.38 ± 0.04
SPG		
high	9.8 ± 0.4	35.40 ± 0.02
low	9.4 ± 0.4	35.36 ± 0.04

Table C4. As for Table C1 but for case study 4.

Case Study 5 (Porcupine Sea Bight)

	T_{bot} (°C)	S_{bot}
AMO		
high	3.7 ± 0.1	35.01 ± 0.01
low	3.6 ± 0.0	35.01 ± 0.01
AMOC (OVIDE)		
high	3.6 ± 0.0	35.01 ± 0.01
low	3.6 ± 0.0	35.01 ± 0.01
NAO		
high	3.6 ± 0.0	35.00 ± 0.01
low	3.6 ± 0.0	35.01 ± 0.01
SPG		
high	3.7 ± 0.1	35.01 ± 0.01
low	3.6 ± 0.1	35.01 ± 0.01

Table C5. As for Table C1 but for case study 5.

Case Study 6 (Bay of Biscay)

	T_{bot} (°C)	S_{bot}
AMO		
high	4.4 ± 0.1	35.07 ± 0.01
low	4.3 ± 0.1	35.06 ± 0.01
AMOC (OVIDE)		
high	4.4 ± 0.1	35.06 ± 0.01
low	4.4 ± 0.1	35.06 ± 0.01
NAO		
high	4.4 ± 0.1	35.07 ± 0.01
low	4.3 ± 0.1	35.06 ± 0.01
SPG		
high	4.3 ± 0.1	35.06 ± 0.01
low	4.3 ± 0.1	35.07 ± 0.01

Table C6. As for Table C1 but for case study 6.

Case Study 7 (Gulf of Cadiz / Alboran Sea)

	T_{bot} (°C)	S_{bot}
AMO		
high	9.4 ± 0.2	36.01 ± 0.06
low	9.4 ± 0.2	36.00 ± 0.09
AMOC (OVIDE)		
high	9.4 ± 0.2	35.99 ± 0.04
low	9.5 ± 0.2	36.04 ± 0.06
NAO		
high	9.5 ± 0.2	36.02 ± 0.05
low	9.3 ± 0.2	35.98 ± 0.06
SPG		
high	9.4 ± 0.2	36.01 ± 0.06
low	9.5 ± 0.2	36.01 ± 0.08

Table C7. As for Table C1 but for case study 7.

Case Study 8 (Azores)

	T_{bot} (°C)	S_{bot}
AMO		
high	2.4 ± 0.0	34.93 ± 0.00
low	2.4 ± 0.0	34.93 ± 0.01
AMOC (OVIDE)		
high	-	-
low	-	-
NAO		
high	-	-
low	-	-
SPG		
high	2.4 ± 0.0	34.93 ± 0.00
low	2.4 ± 0.0	34.93 ± 0.01

Table C8. As for Table C1 but for case study 8. Results for the AMOC and NAO are not included because the mean weighting does not exceed 0.05 for both the high and low period.

Case Study 9 (Reykjanes Ridge)

	T_{bot} (°C)	S_{bot}
AMO		
high	2.9 ± 0.0	34.95 ± 0.01
low	2.9 ± 0.1	34.96 ± 0.01
AMOC (OVIDE)		
high	2.8 ± 0.0	34.94 ± 0.01
low	2.8 ± 0.0	34.94 ± 0.01
NAO		
high	2.9 ± 0.0	34.95 ± 0.01
low	3.0 ± 0.1	34.96 ± 0.01
SPG		
high	2.9 ± 0.0	34.95 ± 0.01
low	2.9 ± 0.1	34.96 ± 0.01

Table C9. As for Table C1 but for case study 9.

Case Study 10 (Davis Strait)

	T_{bot} (°C)	S_{bot}
AMO		
high	3.2 ± 0.1	34.91 ± 0.02
low	3.2 ± 0.1	34.91 ± 0.01
AMOC (OVIDE)		
high	3.1 ± 0.1	34.90 ± 0.02
low	3.2 ± 0.1	34.91 ± 0.01
NAO		
high	3.2 ± 0.1	34.91 ± 0.01
low	3.3 ± 0.1	34.92 ± 0.01
SPG		
high	3.2 ± 0.1	34.91 ± 0.01
low	3.2 ± 0.1	34.91 ± 0.01

Table C10. As for Table C1 but for case study 10.

Case Study 11 (Flemish Cap)

	T_{bot} (°C)	S_{bot}
AMO		
high	2.5 ± 0.1	34.91 ± 0.01
low	2.5 ± 0.1	34.92 ± 0.01
AMOC (OVIDE)		
high	2.4 ± 0.1	34.90 ± 0.01
low	2.4 ± 0.1	34.90 ± 0.01
NAO		
high	2.5 ± 0.1	34.91 ± 0.01
low	2.5 ± 0.1	34.92 ± 0.01
SPG		
high	2.5 ± 0.1	34.91 ± 0.01
low	2.5 ± 0.1	34.91 ± 0.01

Table C11. As for Table C1 but for case study 11.

Case Study 12 (USA Mid-Atlantic Canyons)

	T_{bot} (°C)	S_{bot}
AMO		
high	3.0 ± 0.0	34.95 ± 0.01
low	2.9 ± 0.1	34.96 ± 0.01
AMOC (OVIDE)		
high	3.0 ± 0.0	34.95 ± 0.00
low	3.0 ± 0.0	34.95 ± 0.01
NAO		
high	3.0 ± 0.1	34.96 ± 0.01
low	3.0 ± 0.0	34.96 ± 0.01
SPG		
high	3.0 ± 0.0	34.95 ± 0.01
low	2.9 ± 0.1	34.96 ± 0.01

Table C12. As for Table C1 but for case study 12.

Case Study 13 (European Slope)

	T_{bot} (°C)	S_{bot}
AMO		
high	4.0 ± 0.1	34.98 ± 0.01
low	4.0 ± 0.1	35.00 ± 0.02
AMOC (OVIDE)		
high	3.9 ± 0.1	34.98 ± 0.01
low	3.9 ± 0.1	34.98 ± 0.02
NAO		
high	3.9 ± 0.1	34.99 ± 0.01
low	4.0 ± 0.1	35.00 ± 0.02
SPG		
high	4.0 ± 0.1	34.98 ± 0.01
low	4.0 ± 0.1	34.99 ± 0.01

Table C13. As for Table C1 but for case study 13.

Case Study 14 (North Sea)

	T_{bot} (°C)	S_{bot}
AMO		
high	8.0 ± 0.6	35.21 ± 0.04
low	7.4 ± 0.6	35.17 ± 0.06
AMOC (OVIDE)		
high	7.8 ± 0.7	35.18 ± 0.05
low	7.9 ± 0.6	35.21 ± 0.06
NAO		
high	7.6 ± 0.6	35.14 ± 0.04
low	7.5 ± 0.7	35.14 ± 0.07
SPG		
high	7.9 ± 0.6	35.21 ± 0.05
low	7.4 ± 0.7	35.17 ± 0.06

Table C14. As for Table C1 but for case study 14.

References

- Berx, B., Payne, M., 2017. The subpolar Gyre Index - a community data set for application in fisheries and environmental research. *Earth Systems Science Data* 9, 259-266.
- Buckley, M., Marshall, J., 2016. Observations, inferences and mechanisms of Atlantic Meridional Overturning Circulation variability: A review. *Reviews of Geophysics* 54, 5-63.
- Burkholder, K., Lozier, M., 2014. Tracing the pathways of the upper limb of the North Atlantic Meridional Overturning Circulation. *Geophysical Research Letters* 41, 4254-4260.
- Burkholder, K., Lozier, S., 2011. Subtropical to subpolar pathways in the North Atlantic: Deductions from lagrangian trajectories. *Journal of Geophysical Research Oceans* 116.
- Böning, C., Behrens, A., Getzlaff, K., Bamber, J., 2016. Emerging impact of greenland meltwater on deepwater formation in the north atlantic ocean. *Nature Geoscience* 9, 523-527.
- Böning, C., Scheinert, M., Dengg, J., Biastoch, A., Funk, A., 2006. Decadal variability of subpolar gyre transport and its reverberation in the North Atlantic overturning. *Geophysical Research Letters* 33.
- Curry, R., McCartney, M., 2001. Ocean gyre changes associated with the North Atlantic Oscillation. *Journal of Physical Oceanography* 31, 3374-3400.
- Debreu, L., Vouland, C., Blayo, E., 2008. AGRIF: Adaptive grid refinement in fortran. *Computers and Geosciences* 31, 8-13.
- Dickson, R., Lazier, J., Meincke, J., Rhines, P., Swift, J., 1996. Long-term coordinated changes in the convective activity of the North Atlantic. *Progress in Oceanography* 38, 241-295.
- Duchez, A., Courtois, P., Harris, E., Josey, S., Kanzow, T., Marsh, B., Smeed, D., Hirschi, J., 2016. Potential for seasonal prediction of Atlantic sea surface temperatures using the RAPID array at 26°N. *Climate Dynamics* 46, 3351-3370.
- Enfield, D., Mestas-Nunez, A., Trimble, P., 2001. The Atlantic Multidecadal Oscillation and its relationship to rainfall and river flows in the continental United States. *Geophysical Research Letters* 28, 2077-2080.
- Fischer, J., Visbeck, M., Zantopp, R., Nunes, N., 2010. Interannual to decadal variability of outflow from the Labrador Sea. *Geophysical Research Letters* 37.
- Foukal, N., Lozier, S., 2016. No inter-gyre pathway for sea-surface temperature anomalies in the North Atlantic. *Nature Communications* 7:11333.
- Frajka-Williams, E., 2015. Estimating the Atlantic overturning at 26 N using satellite altimetry and cable measurements. *Geophysical Research Letters* 42, 3458-3464.
- Gary, S., Lozier, S., Böning, C., Biastoch, A., 2011. Deciphering the pathways for the deep limb of the meridional overturning circulation. *Deep Sea Research II: Topical studies in Oceanography* 58, 1781-1797.
- Good, S., Martin, M., Rayner, N., 2013. EN4: quality controlled ocean temperature and salinity profiles and monthly objective analyses with uncertainty estimates. *Journal of Geophysical Research: Oceans* 118, 6704-6716.
- Häkkinen, S., Rhines, P., 2004. Decline of the subpolar North Atlantic circulation during the 1990s. *Science* 304, 555-559.
- Hátún, H., Azetsu-Scott, K., Somavilla, R., Rey, F., Johnson, C., Mathis, M., Mikolajewicz, U., Coupel, P., Tremblay, J.É., Hartman, S., Pacariz, S.V., Salter, I., Ólafsson, J., 2017. The subpolar gyre regulates silicate concentrations in the North Atlantic. *Scientific Reports* 7 (1), 14576.
- Hátún, H., Sandø, A., Drange, H., Hansen, B., Valdimarsson, H., 2005. Influence of the Atlantic Subpolar Gyre on the Thermohaline Circulation. *Science* 309, 19841-11844.

Hosegood, P., van Haren, H., 2004. Near-bed solibores over the continental slope in the Faroe-Shetland Channel. *Deep Sea Research II: Topical studies in Oceanography* 51, 2943-2971.

Hurrell, J.W., 1995. Decadal trends in the North Atlantic Oscillation: Regional temperatures and precipitation. *Science* 269, 676-679.

Johnson, C., Inall, M., Häkkinen, S., 2013. Declining nutrient concentrations in the northeast Atlantic as a result of a weakening Subpolar Gyre. *Deep Sea Research I* 82, 95-107.

Jones, P., Jónsson, T., Wheeler, D., 1997. Extension to the North Atlantic Oscillation using early instrumental pressure observations from Gibraltar and South-West Iceland. *International Journal of Climatology* 17, 1433-1450.

Joyce, T., Deser, C., Spall, M., 2000. The relationship between decadal variability of subtropical mode water and the North Atlantic Oscillation. *Journal of Climate* 13, 2550-2569.

Kerr, R., 2000. A North Atlantic pacemaker for the centuries. *Science* 288, 1984-1985.

Large, W., Yaeger, S., 2009. The global climatology of an interannually varying air-sea flux data set. *Climate Dynamics* 33, 341-364.

Lozier, M., Stewart, N., 2008. On the temporally-varying northward penetration of Mediterranean Overflow Water and eastward penetration of Labrador Sea Water. *Journal of Physical Oceanography* 38, 2097-2103.

Lozier, S., Bacon, S., Bower, A., Cunningham, S., de Jong, M., de Steur, L., de Young, B., Fischer, J., Gary, S., Greenan, B., Heimbach, P., Holliday, N., Houpert, L., Inall, M., Johns, W., Johnson, H., Karstensen, J., Li, F., Lin, X., Mackay, N., Marshall, D., Mercier, H., Myers, P., Pickart, R., Pillar, H., Straneo, F., Thierry, V., Weller, R., Williams, R., Wilson, C., Yang, J., Zhao, J., Zika, J., 2016. Overturning in the Subpolar North Atlantic Program: a new international ocean observing system. *Bulletin of the American Meteorological Society*.

Madec, G., 2008. Nemo ocean general circulation model reference manual. Internal Report LODYC/IPSL, Paris.

Mercier, H., Lherminier, P., Sarafanov, A., Gaillard, F., Daniault, N., Desbruyères, D., Falina, A., Ferron, B., Gourcuff, C., Huck, T., Thierry, V., 2015. Variability of the meridional overturning circulation at the Greenland-Portugal OVIDE section from 1993 to 2010. *Progress in Oceanography* 132, 250-261.

Ruprich-Robert, Y., Msadek, R., Castruccio, F., Yaeger, S., Delworth, T., Danabasoglu, G., 2017. Assessing the climate impacts of the observed Atlantic Multidecadal Variability using the GFDL CM2.1 and NCAR CESM1 Global Coupled Models. *Journal of Climate* 30, 2785-2810.

Scheinert, M., 2008. Causes and impacts of north North Atlantic freshening, University of Kiel.

Smeed, D., McCarthy, G., Rayner, D., Moat, B., Johns, W., Baringer, M., Meinen, C., 2017. Atlantic Meridional Overturning Circulation observed by the RAPID-MOCHA-WBTS array at 26 N from 2004 to 2017. BODC, NERC.

Visbeck, M., Chassignet, E., Curry, R., Delworth, T., Dickson, R., Krahnemann, G., 2013. The ocean's response to North Atlantic Oscillation variability. In: Hurrell, J., Kushnir, Y., Ottersen, G., Visbeck, M. (Eds.), *The North Atlantic Oscillation: Climatic significance and environmental impact*. American Geophysical Union, Washington.

Zantopp, R., Fischer, J., Visbeck, M., Karstensen, J., 2017. From interannual to decadal: 17 years of boundary current transports at the exit of the Labrador Sea. *Journal of Geophysical Research: Oceans* 122, 1724-1748.